3D GRAPHENE-LIKE CARBON STRUCTURE EVOLUTION VIA MICROWAVE PYROLYSIS OF HEMP BIOMASS: A FEEDSTOCK-PROCESS-STRUCTURE-PROPERTY RELATIONSHIP STUDY

by

Farhan Chowdhury Asif

B.Sc. in Mechanical Engineering, Military Institute of Science & Technology, 2019

A Thesis Submitted in Partial Fulfillment
of the Requirements for the Degree of

Master of Science in Engineering

in the Graduate Academic Unit of Mechanical Engineering

Supervisor: Gobinda Saha, PhD, Mechanical Engineering

Examining Board: Rickey Dubay, PhD, Mechanical Engineering, Chair
Clodualdo Aranas, PhD, Mechanical Engineering
Muhammad Afzal, PhD, Mechanical Engineering
Zhibin (Ben) He, PhD, Chemical Engineering

This thesis is accepted by the Dean of Graduate Studies

THE UNIVERSITY OF NEW BRUNSWICK

March 2024

Abstract

Graphene, known for its exceptional properties, faces challenges in broad adoption due to high costs and limited yields, hindering its diverse applications. The utilization of unconventional feedstocks, such as hemp biomass, shows potential for creating a graphene-like carbon (GLC) structure – a close mimic of graphene with prospects for scaling up. This research combines the processing of 'petera' type lignocellulosic hemp biomass with high-temperature thermochemical treatment via microwave pyrolysis. Previous findings from a collaborative study between the UNB Nanocomposites and Mechanics Laboratory (NCM Lab) and the Bioenergy and Bioproducts Research Laboratory (BBRL) indicated a higher carbon fraction presence in hemp-processed biochar structures under medium-temperature microwave pyrolysis (up to 600°C). The current study distinguishes itself by optimizing material design and process conditions, targeting elevated pyrolysis temperatures. The research delves into the mapping of the GLC feedstock-process-structure-property relationship, providing insights into scaling up the results, requiring further process optimization towards industrial applications.

Dedication

To my loving wife, whose unwavering support fuels my journey.

To my parents, whose sacrifices paved the path to this moment.

To my teachers and friends, your encouragement has been my guiding light.

Acknowledgments

In the journey of completing this thesis, I am profoundly grateful for the unwavering support and guidance of Dr. Gobinda C. Saha, my academic supervisor at the University of New Brunswick. Dr. Saha's patient mentorship and encouragement have been instrumental in shaping my academic trajectory, and I am deeply thankful for the myriad opportunities he has provided.

My appreciation also extends to Dr. Muhammad Afzal and the Bioenergy and Bioproducts Research Lab (BBRL) for their invaluable assistance and resources.

Special thanks to Modern Hemp Innovations, Inc. for their 'petera' type hemp stock donation. Gratitude is also owed to the individuals who played indispensable roles during the experimental phase of this thesis. Dr. Felipe Chibante from the Chemical Engineering department greatly facilitated our FT-IR work, while Dr. Lihui Liu's expertise with Raman spectroscopy and Dr. Zhibin (Ben) He's assistance in the elemental analysis was instrumental in our progress. Dr. Mladen Eic and Masoud Haeri's contributions to BET surface area analysis are also deeply appreciated. Special acknowledgment is extended to Steven Cogswell at UNB's Microscopy and Microanalysis Facility for his invaluable assistance with SEM imaging.

I would be remiss not to acknowledge the unwavering support of my lab mates from the NCM Lab—Kelton, Vineeth, Aisa, Arif, and Teck. Their camaraderie and collaboration have made this academic journey both fulfilling and enjoyable.

Table of Contents

List of Tables

List of Figures

Chapter 1

Introduction

1.1 Background of the Study

In the last few years, there has been a tremendous rise in interest in renewable energy sources and sustainable production techniques, aiming to address the looming energy crisis and achieve carbon neutrality. Amidst the great technological advances, the only thing holding us back is the resources available to us. Graphene is regarded as one of the most incredible materials of the 21st century. Graphene is constituted of a single-atom-thick layer of sp^2 hybridized carbon atoms arranged in a hexagonal lattice, which lends its remarkable properties including superior strength, lightness, thermal conductivity, and diffusivity. As a result, graphene is becoming an increasingly desired material constituent in many application areas: photonics, composite materials, coatings, energy harvesting and storage, soil remediation, biomedicine, to name a few. However, the production cost and lower yields of graphene are major obstacles to its industrial appeal. To realize graphene and its carbonaceous cousins' potential researchers have targeted finding economical routes for their manufacturing and eventual scaling up by increasing the process output (yield), yet with the same or better structural caliber at atomic scale.

By the same token, waste biomass is becoming an increasingly target source for creating graphene or graphene-like carbon (GLC) structures as they are abundant, renewable, sustainable with potential for cost reduction and ease of access to market. Among them, lignocellulosic biomass (composed mainly of lignin, cellulose, and hemicellulose) is one of the best potential sources for synthesizing GLC materials. So far, many research groups have used various processes to produce GLC material from biomass. The microwave

pyrolysis method is a particularly popular choice due to its time- and energy-saving attributes, higher heating efficiency, and precision control over the process.

Hemp (a crop enlisted as lignocellulosic biomass) is a versatile, renewable, and sustainable fast-growing crop with strong, flexible fibers, which is relatively easy to cultivate. It is made up of three layers: inner, middle, and outer layers. The inner and outer layers are made up of hemicellulose and lignin, respectively, whereas the middle layer is mostly made up of crystalline cellulose. In Canada, the number of hemp acres that have been sown has grown exponentially since 2009, with 77,800 acres planted in 2018. It is expected that this number will continue to grow in the coming years, and up to 450,000 acres of hemp could be planted in the coming days, potentially resulting in a market value of CAN $1 billion [1].

Disposal of hemp biomass in an environmentally friendly way, however, is a problem that needs to be addressed. Farms across the country are struggling to find space and resources to decompose the stalks (about 70% of the plant) in a sustainable way. Back in 2018, UNB's NCM Lab in collaboration with BBRL embarked on investigating the structural and elemental compositions of biochar created from a medium-temperature microwave pyrolysis of hemp waste biomass. The study for the first time indicated that pyrolyzing hemp yields biochars with a ratio of H:C less than 1.2, possessing a graphite-like structure, as well as showing a downward trend in C/O ratio [2]. The result captured our attention with the possibility of transforming the graphite structure to a GLC or a full-blown graphene structure [3]. Research from other groups has also suggested that hemp can become carbonized when heated, producing nanosheets similar to graphene [4]. Moreover, the use of hemp bast fiber has been employed in several studies to synthesize GLC material

using various techniques [5,6]. Despite this, there are still questions and gaps in knowledge as to what effect feedstock particle size has on the production of GLC material and whether hemp can form GLC material through microwave pyrolysis.

Consequently, the current study was designed to develop a methodology for processing waste hemp biomass in high-temperature microwave pyrolysis condition with the goal to derive a GLC material structure. In doing so, a material design of experiments (DoE) was created with the inclusion of microwave power, residence time, and feedstock particle size as process variables, studying their effects on the characteristics of the evolved GLC. The study utilized quantitative data gathered in a laboratory setting through the application of various analytical techniques, including x-ray diffraction (XRD) analysis, Fourier-transform infrared (FTIR) spectroscopy analysis, BET and N_2 adsorption/desorption isotherm analysis, elemental analysis, and scanning electron microscopy (SEM) analysis.

1.2 Graphene-Like Carbon Materials

Graphene (the fundamental building block for the formation of other carbon allotropes, such as graphene oxide (GO), reduced graphene oxide (rGO), carbon nanotubes (CNTs), carbon nanodots, carbon nanoparticles, and fullerenes) produced using microwave pyrolysis of biomass tend to have disordered layers and defects, such as vacancies, sp^3 carbon, and oxygenated functions. Despite these irregularities, they exhibit most of the properties associated with graphene and can be referred to as GLC materials. Carbon materials derived from biomass with a graphene-like structure feature a great deal of surface area, a porous composition, a relatively high degree of graphitization, and a surface that is chemically stable when the preparation method is carefully regulated.

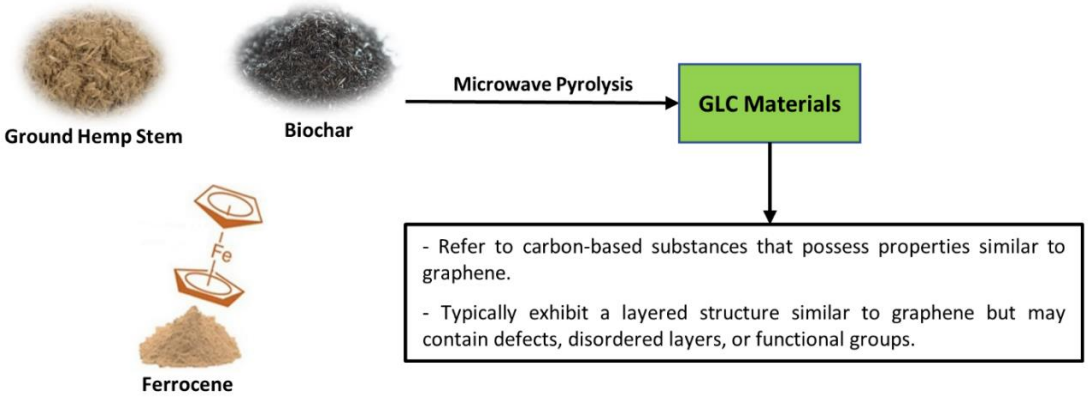

Figure 1: Schematic of GLC material synthesis employed in this study as well as the details of GLC materials.

These materials have the potential of being utilized for energy storage, catalyst technology, biomedical applications, filtration, and multiple other fields [7]. Figure 1 represents the schematic of GLC material synthesis process involved in this study as well as the details of GLC materials.

GLC materials include those based on or containing 0D to 2D forms of graphene, such as modified 2D graphene, graphene derivatives like GO, 1D graphene ribbons, 0D graphene flakes, and multi-layer graphene [8].

Figure 2 shows various carbon allotropes and the molecular structures of graphite, graphene, GO, and rGO.

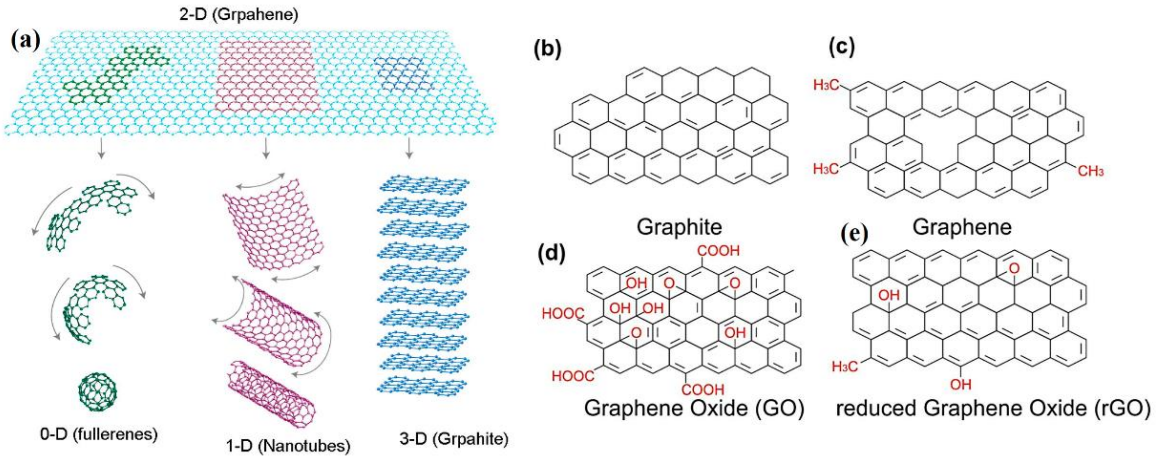

Figure 2: (a) Various carbon allotropes, such as 0D, 1D, and 3D, using 2-D graphene nanosheets as their basic building units; the molecular structures of (b) graphite, (c) graphene, (d) GO, and (e) rGO [9].

1.3 Objectives

The goal of this research is to synthesize GLC material structure from hemp biomass via high-temperature microwave pyrolysis in a N_2 inert atmosphere.

The following objectives outline the scope of this work:

- Synthesize GLC material via microwave pyrolysis of hemp biomass; and
- Evaluate the effect of microwave power, residence time, and feedstock particle size on pyrolyzed product characteristics.

1.4 Significance of the Study

This research is significant because it aims to devise an industrially viable approach to transforming leftover hemp biomass into GLC materials with the use of high-temperature

microwave pyrolysis. Moreover, it is designed to explore how the particle size of the feedstock has an impact on the pyrolysis process as a whole and the characteristics of the pyrolysis product. The knowledge acquired from this study will benefit hemp cultivators, potentially giving them a path forward when it comes to transforming a waste biomass into a value-added product.

1.5 Assumptions

The study operated under the following assumptions:

- The raw material, hemp, had the same composition throughout the experiments.
- The raw material did not contain any impurities after the cleaning process.
- The pyrolysis environment was completely inert.

1.6 Scope and Limitations

The purpose of this study was to assess the feasibility of using hemp as a feedstock for synthesizing GLC structure through microwave pyrolysis. The study focused on examining how the microwave power level, residence time, and feedstock particle size affected the properties and characteristics of the produced GLC materials.

However, this study had certain limitations. For instance, it needed to control other parameters, such as moisture content, batch size, and the concentration of microwave absorber and catalyst, which could potentially impact the final product characteristics. Additionally, measuring reaction temperature reliably posed a challenge. Furthermore, the study did not investigate the individual influence of cellulose, hemicellulose, and lignin on the final product characteristics.

Chapter 2

Literature Review

2.1 Pertinent Literature

Graphene, a one-atom-thick layer (2D) of sp^2-hybridized carbon atoms arranged in honeycomb structures, has attracted great interest from the scientific community because of its unique properties. However, the biggest challenge is the low-cost mass production of graphene with control over properties for desirable applications. Recently, biomass has become an alternative precursor to produce GLC materials. Among them, lignocellulosic biomass is one of the best potential sources as it can produce higher-quality GLC materials with a larger surface area [9]. There are several methods to synthesize graphene, divided into two approaches: top-down and bottom-up. Among those, microwave pyrolysis (a bottom-up approach) is a widely used and cost-effective platform for the thermochemical conversion of biomass into various value-added products.

Until now, researchers have employed a variety of techniques to create GLC materials using microwave pyrolysis of various biomasses. Even though they used various feedstocks and varied process settings, the basic process is nearly identical. The overall process, shown in Figure 3, can be divided into three parts: pretreatment of the sample, pyrolysis of the sample, and post-treatment of the pyrolyzed product.

Pretreatment of the sample consists mostly of washing it with deionized water to eliminate any contaminants, drying it to remove moisture, and grinding it to make a fine powder. For example, Zhang et al. [10] used pine nutshell (PNS) as a feedstock and pyrolyzed it at temperatures ranging from 400 to 700 °C to synthesize hollow carbon nanofibers (HCNFs) on the biochar surface.

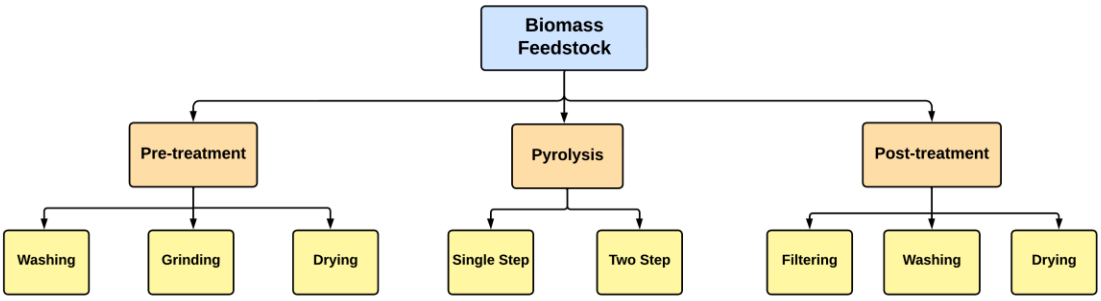

Figure 3: Overall process of GLC material synthesis via pyrolysis.

In the study, the PNS sample was crushed and sieved to a particle size of 65-200 μm before being dried in a vacuum oven at 105 °C for 10 hours to remove moisture. While producing GO from sugarcane bagasse (SB) Debbarma et al. [11] first washed the samples with deionized water and sundried the samples for a few days followed by oven drying at 70 °C for 24 hrs. Yu et al. [12] also oven-dried the cellulose sample for 12 h at 80 °C and produced super-long carbon nanotubes (SL-CNTs) via microwave pyrolysis at 1200 – 1400 °C. Since biowastes are poor microwave absorbers, some studies pretreated the sample and then combined it with microwave absorbers to boost the sample's absorptivity. Zhang et al. [10] combined activated carbon (AC) with dried biomass in an 8:1 ratio. Furthermore, it was discovered that combining a catalyst with the feedstock before pyrolyzing aids in the production of GLC material at a considerably lower temperature. Somanathan et al. [13], Hidalgo et al. [14], and Hashmi et al. [15] used ferrocene as a catalyst during their studies. Somanathan et al. [13] mixed 0.5 g of sugarcane bagasse powder with 0.1 g of ferrocene and heated it for 10 minutes at 300 °C to produce GO. Hidalgo et al. [14] were able to produce CNTs by mixing the sample with ferrocene at a much lower temperature of 600 °C. Hashmi et al. [15] mixed feedstock powder and ferrocene at a ratio of 5:1 and produced

GO at 400 °C. There are also other catalysts used by different researchers, for example, Wang et al. [16] used K_2CO_3 as the activating agent, and Liu et al. [17] used Fe powder at various weight ratios.

The second part of the process is pyrolysis, and it is the main part of the synthesis process where the feedstock decomposes and results in various value-added products. It can be carried out in a single step or two steps. Utilizing a two-step pyrolysis process, Wang et al. [16] carbonized the waste bamboo biomass at 400 °C for 3 h under N_2 gas flow in the first step. After mixing the catalyst with the carbonized product, in the second step, they pyrolyzed at 900 °C for a duration of 25 min under N_2 atmosphere and produced graphene containing biochar. Yu et al. [12] also applied the two-step pyrolysis process where the temperature of the first step of pyrolysis was 600°C, and for the second step, it was 1200, 1300, and 1400°C. They studied the effect of temperature on the synthesized CNTs and observed that the carbon order in the SL-CNTs increased after microwave treatment at 1400 °C. Zhang et al. [10], Debbarma et al. [11], and Gopalakrishnan et al. [18] used the one-step pyrolysis process and studied the effect of reaction temperature on the pyrolyzed product. Zhang et al. [10] found that 600°C was the optimum temperature for the synthesis of HCNFs and at this temperature, a more ordered carbon structure with less organic matrix, functional groups, structural defects, and imperfections was formed. Debbarma et al. [11] observed that 350 °C was suitable for condensation and aromatization of the glucose monomers to form GO nanosheets at a large scale. Gopalakrishnan et al. [18] showed that feedstock containing a variety of minerals can produce porous and large surface areas upon heating and synthesized few-layer graphene like porous carbon nanosheets using ginger as a feedstock which is ideal for the performance of electric

double-layer capacitors. On the other hand, Liu et al. [17] studied the effect of residence time and found that graphene with better quality was obtained after thermal treatment for 90 min when the ratio of carbon source to iron was 3:1, and CNTs were observed after thermal treatment for 105 min. For the post-treatment of the pyrolyzed product, the common methods are filtering, washing with deionized water, and oven drying [11,16,17]. The quality and the characteristics of the product obtained from microwave pyrolysis of biomass mostly rely on the operational conditions and the properties of biomass feedstocks. From the study of Suriapparao et al. [19], it was observed that the microwave pyrolysis reaction temperature is influenced by the feedstock particle size, batch size, and various other parameters. This is essential since controlling the temperature would allow for better control of the gas produced for the synthesis of GLC materials, which is necessary for even nucleation and an even spread of pores. However, the above-mentioned studies did not investigate how the batch size and particle size affected the pyrolyzed product, which could have provided useful information for optimizing the synthesis procedure. Additionally, studies demonstrating the potential for producing GLC material by the pyrolysis of hemp are scarce. Because of this, the goal of this research is to produce GLC materials from hemp using microwave pyrolysis while examining the effects of different process variables, including reaction temperature, residence time and feedstock particle size, on the final product's quality and properties.

2.2 Pyrolysis Process

Pyrolysis is a type of thermochemical conversion process that takes place without the presence of oxygen and is designed to break down the chemical bonds in a particular feedstock to decompose organic materials. This yields biochar, bio-oil, syngas, and other value-added products. The process is conducted in an oxygen-free environment with temperatures ranging between 400°C and 1200°C or even higher. In this environment, biomass can be heated beyond its thermal stability limit without initiating combustion. Pyrolysis is a complex process involving various reactions and pathways such as depolymerization, dehydration, decarboxylation, intramolecular condensation, and aromatization, which take place at different temperatures and yield diverse product states for lignocellulosic components [9].

Depending on the heating mechanism used, pyrolysis can be classified into two categories: conventional pyrolysis (CP) and microwave-assisted pyrolysis (MAP). CP usually relies on an electric heating mechanism, which is often inefficient and energy intensive. MAP, on the other hand, has gained considerable attention from the research community due to its advantages over CP. MAP is faster, more energy-efficient, and offers greater precision over the process. Furthermore, MAP also results in higher heating rates and yields of desired products compared to CP [9].

2.3 Key Distinction Between MAP and CP

Robinson et al. [20] conducted a study that combined microwave pyrolysis, dielectric measurement, and fluid flow modeling to better understand the differences between microwave and conventional pyrolysis. Through their research, they were able to analyze

and contrast the mechanisms of both processes. The key finding is that the distinction is not between microwave and conventional heating, but rather between low and high heating rates. With low microwave power or domestic ovens, the heating rate can be comparable to conventional methods. When heating rates are low, vaporization of water within biomass structure is slow and pressure remains close to atmospheric. Pyrolysis in this case would proceed similarly to conventional methods with hemicellulose depolymerizing at temperatures over 200°C, cellulose at 300°C, and lignin in 220-400°C range with diverse chemical composition produced. When heating rates are high (microwave heating), the vaporization rate increases leading to pressure build-up which elevates the boiling point of water remaining within biomass at temperatures well over 100°C. This results in hydrolysis of hemicellulose at ~130°C producing furfural as primary product; hydrolysis of cellulose occurs at ~175°C producing levoglucosan as primary product; And lignin follows the same reaction scheme as conventional pyrolysis due to its lack of hydrolysable linkages upon further heating [9], as illustrated in Figure 4.

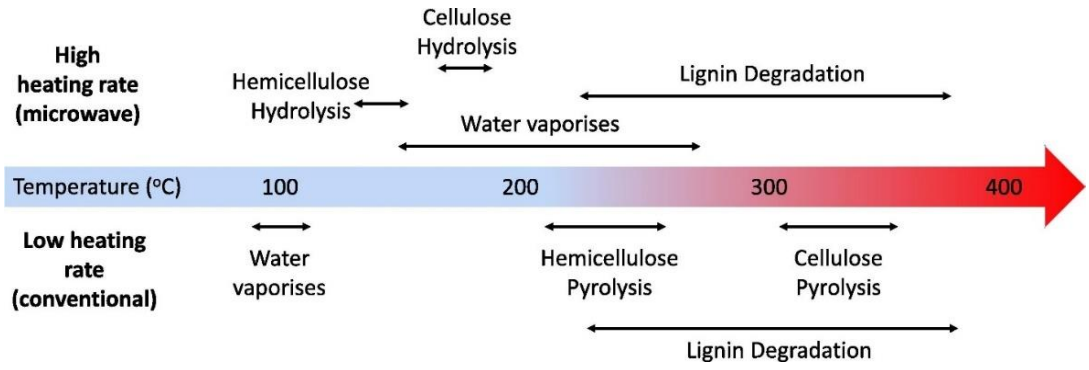

Figure 4: Scheme for MAP and CP [20].

It was hypothesized that different behaviors with different biomasses occur not because of inherent chemistry but due to their micro- and macro-structure which is characterized by permeability - high permeability would not sustain high pressures so no difference between microwaves vs convectional would be expected; Whereas low permeability does sustain those pressures allowing for a difference in mechanistic pathway based on heating rate. The key finding of Robinson is also evident from the study of Zoraida et al. [21] who used anthracene oil as raw material for the production of carbon precursors via conventional and microwave technologies. In addition, they observed that the energy usage of microwave-assisted technology for producing these materials was up to 60% lower than traditional heating. The graphite's obtained from microwave-based precursors had an excellent degree of graphitization, with smaller crystallite sizes than those from an exclusively microwaved coke. Graphene materials synthesized from these microwave precursors showed improved lattice recovery, structure, and reduced oxygenated surface functional groups, especially when derived from microwave-derived coke [9].

2.4 Microwave Pyrolysis Reaction Mechanism

In CP, the heat is transmitted from an external source to the material's exterior and then to its core through conduction, convection, and radiation. Therefore, CP is inefficient, energy-consuming, and relies on convection and thermal conductivity of the material being processed. In contrast, electromagnetic energy is transformed into heat energy in MAP. This occurs by microwaves entering the feedstock and then being stored as energy, which is then converted into heat inside the feedstock's core. This method is advantageous because it avoids heat losses due to volumetric heating of the feedstock [9].

In MAP, the temperature of the biomass particle increases from the interior to the exterior, but in CP, it is the opposite. Furthermore, for both MAP and CP, the diffusion of volatile materials (mass flow) is always outward. Thus, heat flow and mass flow are concurrent for MAP and countercurrent for CP as shown in Figure 5. While the volatile elements diffuse from the interior core of the feedstock to its exterior surface, the surrounding of the feedstock is extremely hot during the CP process, and relatively cooler for the MAP process. As a result of the improved heating mechanisms described above, MAP's heating and response mechanisms have significant advantages over CP. Benefits of using MAP include increased heating rate, non-contact heating, uniform heating, energy transfer rather than heat transfer, reduced thermal inertia, more heating efficiency, less feedstock pre-treatment, faster response time, improved control, safety, and so on. Because MAP speeds up thermochemical processes and shortens the reaction time, it also has the added benefit of reducing energy consumption [9].

Also, it is worth noting that biomass does not absorb microwaves well, and therefore does not reach the necessary temperatures for pyrolysis when exposed to microwaves. Thus, pyrolysis systems employ external microwave absorption materials [9].

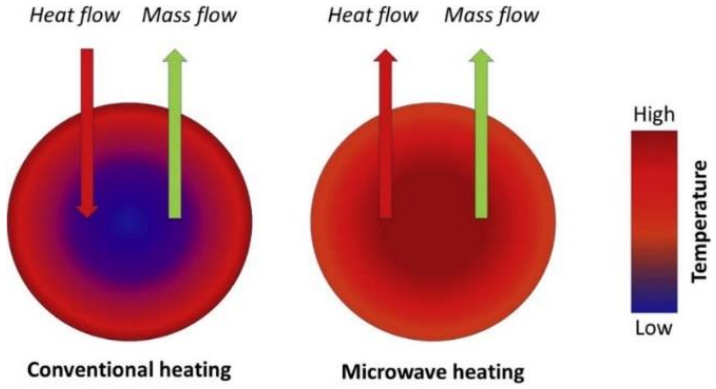

Figure 5: Illustration of the differences between microwave and conventional heating techniques [22].

2.5 Effect of Microwave on GLC Materials Synthesis Via Pyrolysis

In the process of GLC materials synthesis via pyrolysis, the choice of heating method plays a key role in determining the amorphous phase transition of graphene. Direct pyrolysis via traditional heating methods typically results in an amorphous phase and small graphite clusters. On the other hand, microwave heating can be used to convert electromagnetic energy into heat energy at the molecular level, leading to the creation of localized hotspots with a much higher temperature than the bulk material. These hotspots act as nucleation sites, which promote the rearrangement of molecules from an unordered phase to a crystalline phase. Furthermore, microwave radiation treatment can be used to transform sp^3 bonds to sp^2 bonds, in preparation for graphene formation. Additionally, this method can improve the degree of graphitization of carbon material at a lower temperature in a shorter period without the need for a catalyst, while also producing a higher yield of few-layer graphene compared to conventional heating techniques [9]. A better understanding of the effect of microwave on the synthesis of carbon-based materials could be gained from the study of Omoriyekomwan et al. [23] and Kaiqi et al. [24].

Omoriyekomwan et al. [23] conducted a study where they compared the results of forming hollow carbon nanofibers (HCNFs) via microwave pyrolysis of palm kernel shell at 500 °C and 600 °C to those synthesized with fixed-bed pyrolysis. They observed that the development of HCNFs could only be detected during microwave pyrolysis, implying that microwave radiation played a significant role in the production of these nanostructures. This growth was believed to be due to the microwave radiation being absorbed by the biomass, causing an electric arc formation and devolatilization. The heavy components of the volatile matter then resolidified on the surface as a result of lower temperatures,

forming carbon nanospheres. These nanospheres then self-extrude outward from the biomass particle through nano-sized channels, initiating HCNF growth, which is known as the "self-extrusion model growth". In comparison, when conventional heating was used in fixed-bed pyrolysis, the surrounding temperature was higher than the particle core, preventing volatiles from solidifying and undergoing secondary cracking instead.

Kaiqi et al. [24] synthesized multi-walled CNTs via microwave-induced pyrolysis of gumwood. In this experiment, gumwood was pyrolyzed at 500 °C and maintained for 30 minutes under an oxygen-free atmosphere with nitrogen gas flowing at a rate of 100 mL/min. The gumwood was then combined with SiC in a 20:1 mass ratio, and the resultant compounds were separated for further analysis. For comparison, conventional pyrolysis was also performed at the same temperature and nitrogen flow rate. In terms of morphology and microstructure, they observed that the chars formed by microwave-induced pyrolysis differed from those produced by conventional pyrolysis, with the latter having no CNTs on their surface. They attributed the formation of CNTs under microwave-induced pyrolysis to the special effect of microwave radiation on the thermochemical processing of biomass. They proposed a mechanism for CNT development under microwave irradiation, in which volatiles released from biomass formed char particles, which then served as substrates. Mineral matter in char particles served as a catalyst, while released volatiles served as a carbon source gas, undergoing thermal and/or catalytic breaking on char particle surfaces. As a result of the impacts of microwave irradiation, amorphous carbon nanospheres formed, which then self-assembled into multi-walled CNTs. This method has the benefit of producing localized hot spots that could graphitize CNTs at far lower temperatures than conventional heating. The advantage of this approach was that it efficiently produces

localized hot spots that graphitized CNTs at much lower temperatures than conventional heating requires [9].

2.6 Correlation Between MAP Process Conditions and Pyrolyzed Product Characteristics

Microwave pyrolysis depends on the interaction between feedstock and microwave irradiation. The quality and features of the product obtained from microwave pyrolysis of biomass mostly rely on the operational conditions and the properties of biomass feedstocks. In this section, we explore the relationship between the various process parameters of pyrolysis and their effect on the final pyrolyzed product, with the goal of providing insight into how to optimize the production of GLC materials.

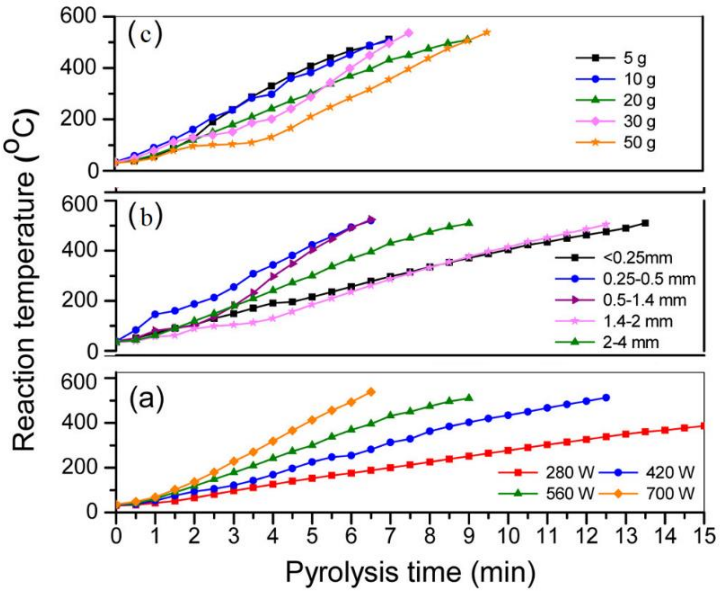

Figure 6: Reaction temperature profiles for various circumstances of microwave pyrolysis (a) Microwave power effect, (b) effect of particle size, (c) effect of initial mass [19].

The performance of microwave pyrolysis is greatly affected by the microwave power, particle size, and batch size of the feedstock as shown in Figure 6.

Figure 6a illustrates that increasing the microwave power increases both the heating rate and the maximum reaction temperature. Additionally, reducing the particle size also increases both the heating rate and maximum reaction temperature, as shown in Figure 6b. This can be attributed to increased bulk density and intra-particle contact area with reduced particle size [25].

Furthermore, reducing the particle size to a specific size (e.g., less than 0.25mm) has been observed to prevent heat from transferring within the particles, thus slowing the process of pyrolysis [19]. Parthasarathy et al. [26] found that increasing the feedstock particle size increases both the char yield and carbon content of the char. Lastly, the batch size of the raw material has been found to play a crucial role in microwave pyrolysis. Figure 6c shows that using a small amount of starting material (5g-15g) yields higher heating rates and higher residence temperatures at a much lower microwave power [27,28].

Low initial moisture levels in biomass are usually preferable for the pyrolysis process. Drying the biomass before subjecting it to pyrolysis improves the energy efficiency of the process [29]. Demirbas observed that increasing moisture content decreases biochar yield and increases the yield of liquid product [30]. However, a few studies have found that increasing the moisture level of the feedstock leads to an increase in char and gas generation [31–33]. Also, the reaction temperature decreases as the moisture content increases, because when the mixture is heated up, heat is expended in the process of drying out the components [34]. Darmstadt et al. [35] observed that feedstock moisture content had a greater impact on softwoods than hardwoods. In addition, Xiaodi Li et al. [36]

investigated the effects of preheat temperature on pyrolysis properties and product properties, finding that preheating the feedstock before microwave pyrolysis increases biochar yield, shortens the initial time for rapid temperature rise, and increases the BET surface area. The effect of thermal pretreatment was also reported by Jian et al. [37]. Feedstock moisture content also influences the heating rate. A lower heating rate arises from higher moisture content [38]. Additionally, it was noted that as initial moisture content increased, the specific char surface area increased, though the effect was more pronounced at lower pyrolysis temperatures [39]. Furthermore, it is common practice to dry biomass feedstock prior to pyrolysis, and the feedstock is frequently dried to a moisture level of less than 10% [40].

The reaction temperature of pyrolysis has a significant impact on the char yield and characteristics. According to Mohammad et al. [41], the char yield reduces as the pyrolysis temperature rises. At higher temperatures, the devolatilization process accelerates, which leads to more vapors and gases being produced and a decrease in the char yield [42]. With the help of Raman spectroscopy Asadullah et al. [43] observed that an increase in temperature causes char to aromatize more quickly. The maximum pyrolysis temperature also affects the surface area, pore structure, and carbon content. According to one study, the BET surface area of a char decreases as the pyrolysis temperature rises. This was found to be quite drastic, with the surface area dropping by a minimum of 200 times when the temperature was raised from 500 to 800°C. It is believed that the drastic reduction in micropores which occurs between 500°C and 800°C is what caused the sharp decline in the surface area [39]. In a different analysis, Fu et al. [44] observed that the surface area of char increases with temperature, however, it decreases slightly if the temperatures surpass

1173 K. Zhao et al. [45] also found that pyrolyzing the rapeseed steam from 200 to 700 °C resulted in an increase in surface area, from 1 to 45 m^2/g, which shows more of a carbonaceous, aromatic structure for the biochar. This behavior can be attributed to the release of volatile gases and the formation of pores at higher temperatures. Furthermore, Lua et al.'s [46] research indicates a general correlation between the BET surface area, micropore surface area, and total pore volume, which increases up to a specific temperature and then begins to decrease gradually. The initial increasing trend could be attributed to the emission of low-molecular-weight gases from the carbon structure. The declining trend might be related to the weakening and liquifying of some of the residual volatiles in the chars, which causes an intermediate melt to form in the chars. This intermediate melt obstructs the formation of the char's primitive pore structure by partly sealing some of the pores. Nevertheless, when the pyrolysis temperature was increased further, it caused the pores to grow and develop, thus leading to an increase in the BET surface area, the micropore area, and the total pore volume. The char's intermediate melt undergoing depolymerization and evaporating is the reason behind this phenomenon, which causes the previously sealed pores to open up, as well as the formation of new pores as a result of the disappearance of the heavier volatiles. As the pyrolysis temperature increased further, a decrease in BET surface area, micropore surface area, and total pore volume were observed. This was likely due to the compression of pores within the char and the narrowing of the pore openings, which both cause the accessible pore surface area to be reduced. Another potential factor might be the production of secondary melt from high molecular weight volatiles, comparable to the previously stated intermediate melt. The fixed carbon content and carbon content of char increase with temperature as a result of

deoxygenation and dehydration, indicating greater structural ordering for lowering reaction site concentration [45,47,48]. Also, with increasing pyrolysis temperature the total volume of pores increases, but the average pore diameter decreases as a result of an increase in the proportion of relatively tiny pores [45].

The char characteristics and yield are significantly influenced by the heating rate as well. According to Mohammad et al. [41], the char yield reduces as the heating rate rises. Although the influence of the rate of heating was more noticeable at higher temperatures when it came to the production of char [49]. However, compared to char produced at low heating rates, high heating rate char has a smaller surface area [44]. It is believed that this is due to an excessive heating rate that raises the temperature of the char interior and results in partial graphitization and the construction of graphene structure, neither of which contributes to the development of a large surface area. On the contrary, Zhao et al. [45] found that rapeseed stem surface area increases at first with the increasing heating rate due to a larger extent of thermal decomposition and then lightly decreased. When the heating rate is increased, the carbon content of char decreases slightly while the hydrogen and oxygen content increases. Additionally, at elevated temperatures, the heating rate impact starts to disappear [50].

Moreover, Parthasarathy et al. [26] reported that the duration of residence in a given environment has an impact on char yield and its carbon content. They observed that increasing the residence period reduces char production while increasing char carbon content. By decreasing the char yield, a longer residence period allows for more time for the reactants in the volatiles to interact with the char and lead to a higher gas yield. Better devolatilization is achieved with a longer residence time, which increases the char's carbon

content. Also, research has demonstrated that the BET surface area of the char has a direct correlation with the residence time. Initially, the BET surface area increases with the increase in residence time, but this effect levels off after prolonged times. This can be attributed to the sigmoidal-shaped curve of the devolatilization rate [51]. Zhang et al. [52] also observed that the BET surface area of chars increased with the residence time until a certain point, after which it began to decrease. This can be explained by the fact that chars' ability to generate pores might benefit from a fair extension of residence time at high temperatures. However, if the residence period is prolonged too much, the pore structure of the chars may be destroyed, which would then cause deactivation.

Lastly, the use of microwave absorbers to indirectly heat biomass particles during pyrolysis has been shown to increase the reaction temperature at relatively low microwave power. This increase in temperature has a significant effect on the yield and quality of the pyrolysis products [53]. In addition, the use of iron-based catalysts, such as ferric chloride or ferrocene, can help to produce high-quality graphene-like biochar with excellent physicochemical properties. Furthermore, by using ferrocene as a catalyst, it is possible to produce GO at a much lower temperature [9,14,15,54].

2.7 GLC Material Structure Formation Mechanism

Most of the biomass is lignocellulosic and contains long chains of carbon, hydrogen, and oxygen compounds. The process of converting lignocellulosic biomass into graphene involves increasing the carbon content and arranging the carbon structures in a graphitic-like form. This process involves two steps: carbonization and graphitization. Carbonization involves the removal of light molecular weight compounds through heating, while

graphitization is used to arrange the remaining carbon structures into a graphitic-like form. The converted carbon structure may not be similar to pure graphene, but the properties that they possess are somewhat graphene-like [55].

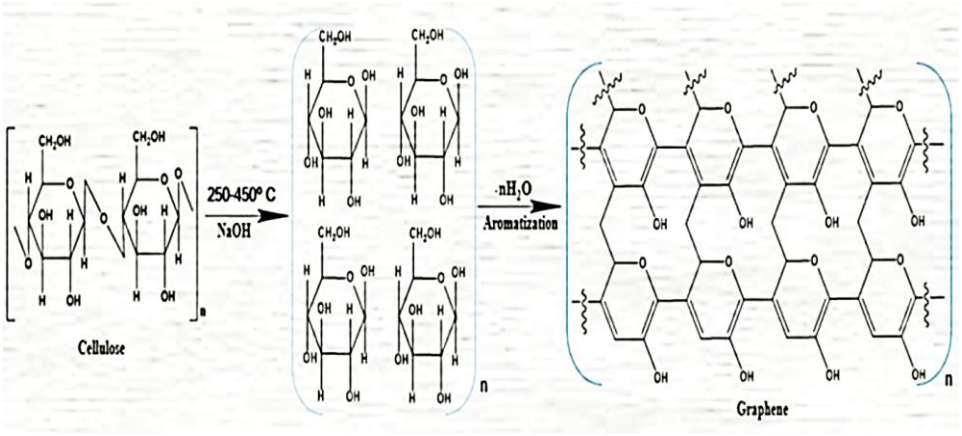

Figure 7: Mechanism of formation of graphene nanosheets at 250-350°C [56].

Debbarma et al. [56] synthesized graphene nanosheets from sugarcane bagasse via pyrolysis in the presence of sodium hydroxide. The chemistry behind the formation of graphene nanosheets is presented in Figure 7.

Sugarcane bagasse has a high concentration of cellulose, which is composed of glucose monomers held together by glycosidic bonds. During the pyrolysis of sugarcane bagasse, the breakdown of glucose monomers takes place, and these monomers contain aldehyde and hydroxyl groups. The hydroxyl group on the fifth carbon of the glucose molecule can then bind to the aldehyde group on the first carbon to form a cyclic hemiacetal structure. This structure is similar to pyran and consists of six-membered heterocyclic rings. It is thought that many of the glucose monomers were linked via glycosidic bonds during

pyrolysis, and further condensation and aromatization of the cyclic rings occurred to form planar graphitic polyaromatic ring structures.

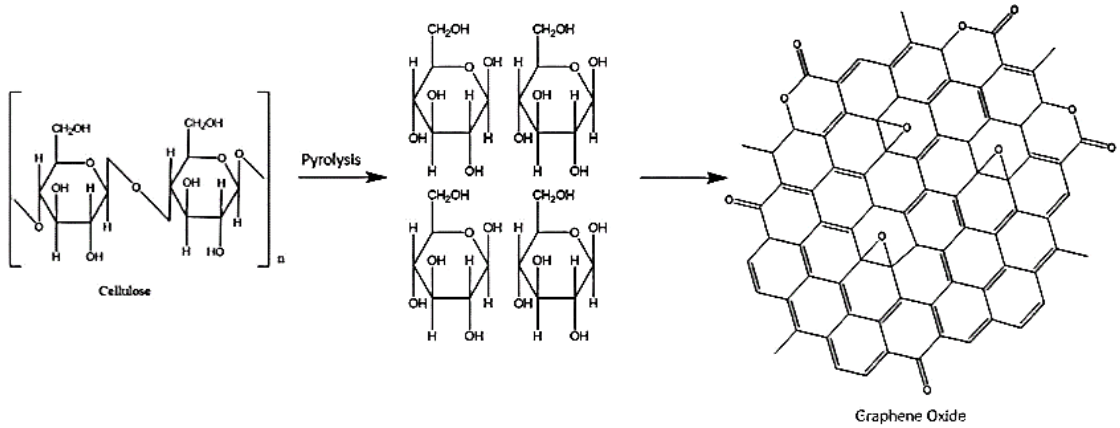

Figure 8: Mechanism of formation of GO from sugarcane bagasse [11].

Debbarma et al. [11] also synthesized GO from sugarcane bagasse where heating sugarcane bagasse at different temperatures caused the degradation of glucose monomers, leading to the formation of glycosidic bonds and polyaromatic rings. The presence of air facilitated oxidation, aromatization, and condensation, resulting in the formation of SBGO nanosheets. The mechanism is depicted in Figure 8.

This same research group synthesized nitrogen doped GO (N-GO). The formation mechanism was the same as stated above. Primary amine groups from the amino acids enhanced the nitrogen content.

This resulted in the formation of N-GO, as illustrated in Figure 9 [57].

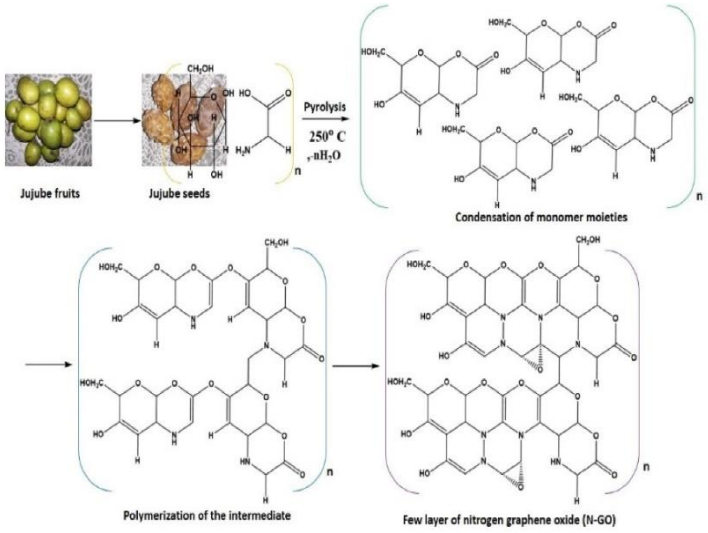

Figure 9: Mechanism of formation of N-GO [57].

Roy et al. [58] developed a method for synthesizing graphene from tannic acid, alginic acid, and green tea by a controlled pyrolysis procedure and proposed a formation mechanism of graphene from alginic acid, illustrated in Figure 10.

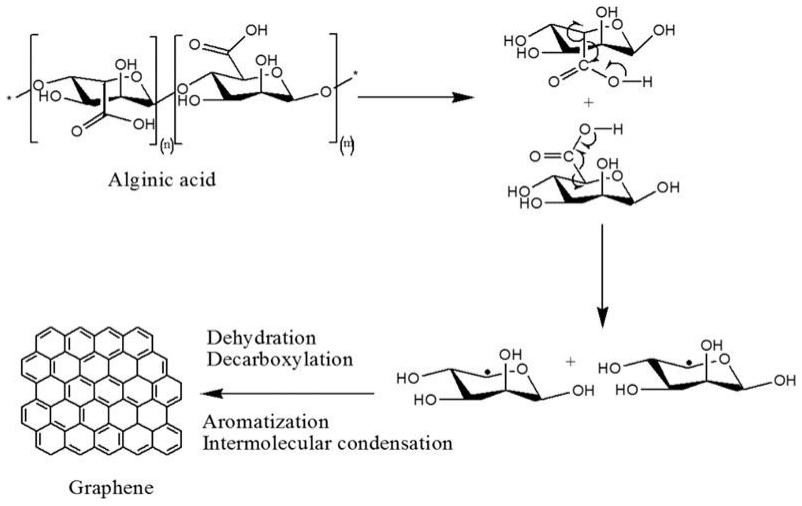

Figure 10: Pyrolysis reaction mechanism for graphene synthesis from alginic acid [58].

They proposed that this reaction likely started with the production of radicals, which was then followed by the release of water molecules and CO_2 and the aromatization and intermolecular condensation reactions at the temperature of 1100°C. They hypothesized that similar processes happened with the polyphenols from green tea and tannic acid based on the presence of carboxyl groups and vulnerable oxygen bonds in their molecular structures.

Omoriyekowan et al. [59] explored the process of CNTs formation with the most recent investigation, synthesizing CNTs with cellulose taken from PKS. In order to draw out the bio-components from the PKS, two distinct techniques were utilized. Once the extraction process had concluded, cellulose and lignin were then exposed to microwave pyrolysis. The end result of their research suggested that cellulose played a vital part in generating CNTs. Figure 11 illustrates the reaction pathways of the decomposition of cellulose to produce nanotubes. The authors examined bio-oils derived from lignin and cellulose to better understand the role of cellulose. Bio-oils derived from cellulose were high in monosaccharides, while bio-oils derived from lignin were rich in phenols and single-ring hydrocarbons. According to the authors, the breakdown of cellulose resulted in the production of monosaccharides such D-glucopyranose, which was employed as a carbon source for CNTs synthesis. Splitting of the glycosidic bonds in D-glucose generated anhydrides, oligosaccharides, and levoglucosan. Subsequently, these elements underwent degradation, cleavage, and rearrangement, leading to the formation of anhydro sugars and levoglucosan. The splitting of the C-O bonds in levoglucosan was followed by its aromatization, resulting in a formation of graphite layers, as shown in Figure 11.

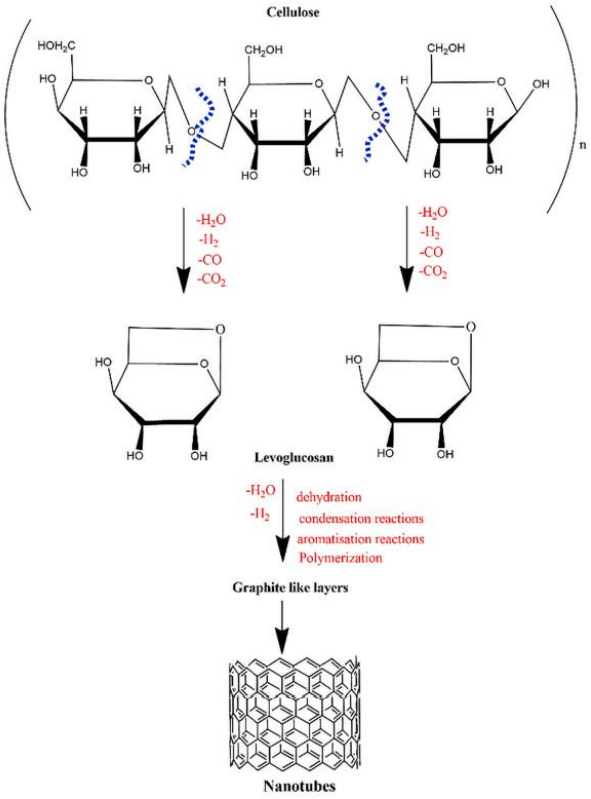

Figure 11: Reaction pathways during the decomposition of cellulose [60].

Liu et al. [17] manufactured graphene using commercially accessible kraft lignin (KL) and carefully examined the formation process, structure, and features. They provided a general mechanism of lignin-based graphene that was catalyzed by iron. The main reactions were pyrolysis and carbonization of KL at temperatures between 250 and 500 °C where polyolefin compounds were converted into amorphous carbon (a-C) with the aid of iron particles via catalytic dehydrogenation. The a-C was in a metastable state and possesses a large amount of energy, so it requires less energy to dissolve in iron metal than C atoms. The temperature required for carbon to dissolve into iron is 570 °C. Through the precipitation dissolution mechanism, a-C diffused into the metal particle and then precipitated as graphene on the free surface when the solid solubility limit was reached

during cooling. Smaller metal particles and longer annealing times resulted in the migration of activated carbon species to the top surface and the nucleation of graphene. Graphene was observed when the holding time was in the range of 90-105 minutes, but had notably reduced areas and less graphene been identified by Raman when the holding time was longer than 105 minutes. The probable cause of this was the growth of a sp^2 carbon network along the surface of the iron particles, which accumulated into a graphite shell. Additionally, the contact between the a-C and iron particles at higher temperatures resulted in a catalytic graphitization process. Iron has the ability to catalyze graphitization even at a low temperature due to the decomposition of iron carbide in the insulation stage.

The reaction equations were as follows:

$$Fe + C_a \rightarrow Fe_3C$$

$$Fe_3C \rightarrow Fe + C_g$$

where C_a is amorphous, and C_g is graphitic carbon.

The general lignin-based graphene synthesis mechanism is illustrated in Figure 12.

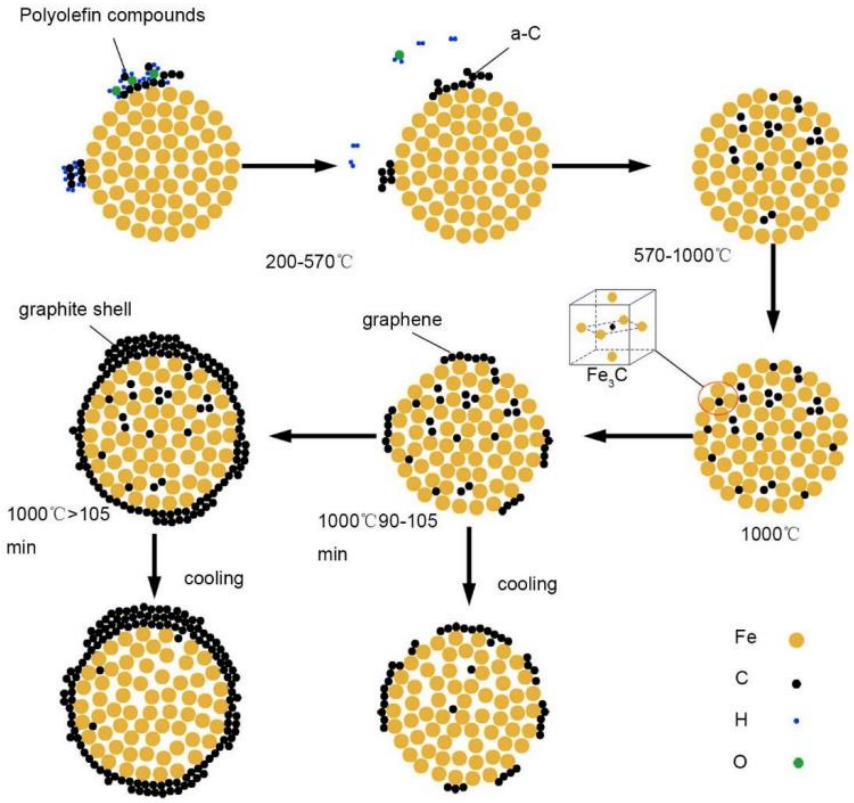

Figure 12: Schematic representation of the graphene synthesis processes from KL using iron particles as catalysts [17].

The newly produced carbon from the breakdown of iron carbide is active and can be quickly transformed into graphite. On the other hand, too much iron may make the decomposition of Fe_3C more challenging. The formation of graphene is carried out in two phases when iron particles are used as a catalyst. One of these is the precipitation and dissolution of carbon atoms, while the other is the manufacture and disintegration of iron carbide. As a consequence, the retention time has an influence on the formation of graphene [9].

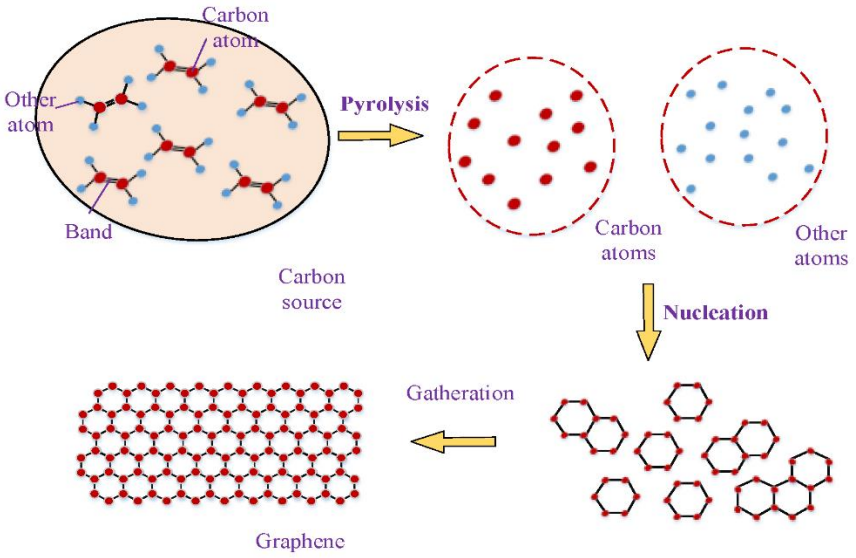

Figure 13: Mechanism of graphene formation via pyrolysis process [61].

Reviewing all the mechanisms discussed above, it may be concluded that the pyrolysis process involves the splitting and recombination of molecules. Carbon atoms form single covalent sp^3 bonds with other atoms, but during the graphene formation process, these bonds are broken, allowing the carbon atoms to form sp^2 bonds in the form of benzene rings. This process of nucleation leads to the development of graphene, as illustrated in Figure 13.

2.8 Suitable Feedstock for GLC Material Structure Synthesis via Pyrolysis

Recent research has focused on synthesizing graphene or GLC material from various biomass sources as a sustainable, non-toxic, environmentally friendly alternative to traditional materials. Lignocellulosic biomass has been identified as a particularly promising source for GLC materials with a large surface area. Table 1 provides data on the elemental and proximate analysis of various bio precursors used to synthesize graphene

through various methods. It suggests that feedstock with higher carbon content is ideal for GLC material synthesis via pyrolysis. Moreover, the characteristics of the final product are determined more by the synthesis method than the feedstock material.

Table 1: Elemental and Proximate Analysis of various bio precursors [9].

Sample	**Proximate analysis, wt.%**				**Ultimate analysis, wt.%**			
	Moisture content	**Volatile matter**	**Fixed carbon**	**Ash**	**C**	**H_2**	**N_2**	**O_2**
Softwood	11.5	67.3	19.5	1.7	44.43	6.16	0.18	49.23
Hemp	10.7	69.6	18.8	0.9	45.71	5.89	-	48.40
Rice straw	8.25	72.20	14.44	13.36	45.41	6.28	0.99	47.11
Pine nutshell	2.12	74.53	22.63	0.94	50.16	5.81	0.28	43.41
Palm Kernel Shell	14.90	74.68	23.68	1.64	49.90	5.25	0.36	43.54
Populus wood	-	-	-	-	39.75	6.09	1.52	52.54
Spent Coffee Beans	-	-	-	-	49.30	3.61	2.24	41.33
Rice husk	6.81	59.8	13.68	19.71	40.71	4.97	0.49	-
Sugarcane bagasse	9.51	74.98	13.57	1.94	43.77	6.83	-	47.46
Orange Peel	-	-	-	3.05	49.59	6.95	0.66	39.7

Each component of lignocellulosic biomass decomposes differently, and the breakdown is affected by temperature, heating rate, and the presence of contaminants. The three

components disintegrated at various temperatures, with hemicellulose being the one that would pyrolyze the most easily. Due to the intricate structure and higher resistance to elevated temperatures than hemicellulose and cellulose, lignin would be the most challenging to pyrolyze. Studies on the impact of cellulose, hemicellulose, and lignin content on the formation of GLC material via pyrolysis are scarce. Therefore, future studies may concentrate on the impact of various lignocellulosic components on the quality of the GLC materials produced through pyrolysis process [9]. The lignocellulosic content of several bio precursors previously employed to synthesize GLC material is shown in Table 2.

Table 2: Lignocellulosic Content of various bio precursors [9].

Biomass	**Cellulose (wt%)**	**Hemicellulose (wt%)**	**Lignin (wt%)**
Hemp	53-91	4-18	1-17
Rice Husk	32.67	31.68	18.81
Sugarcane Bagasse	50	25	25
Empty Fruit Bunches of Palm Oil	37.26	14.62	31.68
Wheat straw	34.40	20-25	20
Palm Kernel Shell	27.7	21.6	44
Bamboo	47.2	23.9	25.3
Rice Straw	29.2-34.7	12.0-29.3	17.0-19.0
Switch Grass	30-50	10-40	5-20
Miscanthus	24	44	17

2.9 Key Takeaways from Literature Review

The review comprehensively covers recent studies, microwave pyrolysis reaction mechanisms, factors influencing the production as well as the characteristics of GLC materials, suitable feedstock types, and formation mechanisms.

Several noteworthy aspects emphasized in the literature review comprise:

- Graphene possesses unique properties but faces challenges in cost-effective mass production.
- There are currently no studies demonstrating the feasibility of synthesizing GO from hemp waste biomass.
- Knowledge gaps exist regarding process parameters' impact on GO characteristics, particularly feedstock particle size.
- Biomass, especially lignocellulosic sources, is promising for GLC materials synthesis.
- Microwave pyrolysis is widely used for biomass conversion into value-added products due to its cost-effectiveness and versatility.
- The synthesis process of GLC material typically involves sample pretreatment (washing, drying, grinding), pyrolysis, and post-treatment (filtering, washing, drying).
- Catalysts like ferrocene are often used to enhance efficiency, while microwave absorbers are employed to boost sample absorptivity.

- Biomass undergoes a two-step process involving carbonization and graphitization to convert into GLC materials.
- Understanding the correlation between microwave pyrolysis conditions and product characteristics is crucial for optimizing GLC material production.

Overall, the literature review provides valuable insights into synthesizing GLC materials via microwave pyrolysis and emphasizes the importance of optimizing process parameters to tailor the final product properties for specific applications.

Chapter 3

Methodology

The study was designed to synthesize GLC material from waste hemp biomass via microwave pyrolysis and to investigate the effects of different process parameters on the characteristics of the synthesized product. The variables involved in this study are listed in Table 3.

Table 3: Different variables of this study.

Independent Variables	Microwave Power, Residence Time, Feedstock Particle size
Dependent Variables	Product Yield, I_D/I_G ratio, Structural parameters, Functional groups, BET surface area, Pore volume, Elemental composition, Surface morphology.
Control Variables	Moisture Content, Batch size, Feedstock, Feedstock: CMWA, Catalyst, and concentration.
Confounding Variable	N_2 gas pressure/Flow rate, Magnetron cooling water temperature, Humidity, Room temperature

3.1 Materials

The "Petera" type Hemp stem, donated by Modern Hemp Innovations, was used as biomass feedstock for microwave pyrolysis experiments. Since biomass is not a good microwave receptor, previously produced biochar from the hemp stems was used as a microwave

receptor to achieve reaction temperatures under microwave irradiation. Ferrocene 99% [$Fe(C_5H_5)_2$] from Fisher Scientific was used as a catalyst in this study.

3.2 Design of Experiments

The study investigated the influence of three variables, namely microwave power, residence time, and feedstock particle size, on the characteristics of the pyrolyzed product. Each experiment was conducted three times, and each variable had two levels. A 2^3 full factorial design was employed for the study. The experimental design, generated with Minitab, aimed to randomize the trials, minimizing the effects of confounding variables and bias. Specifics of the experimental design are outlined in Table 4.

Table 4: Design of experiments.

Experiment No	Microwave Power (W)	Residence Time (min)	Particle Size (µm)
1	600	60	425-600
2	600	90	300-425
3	600	90	425-600
4	900	90	300-425
5	600	90	300-425
6	900	60	300-425
7	600	60	425-600
8	900	90	300-425
9	900	60	425-600
10	900	60	425-600

11	600	60	300-425
12	900	90	300-425
13	600	90	300-425
14	900	90	425-600
15	600	60	300-425
16	900	60	300-425
17	600	60	425-600
18	600	90	425-600
19	600	90	425-600
20	600	60	300-425
21	900	90	425-600
22	900	90	425-600
23	900	60	425-600
24	900	60	300-425

3.3 GLC Material Production

This section outlines the steps involved in producing GLC material via microwave pyrolysis. There were two stages to each experiment, which could be defined as sample preparation, and microwave pyrolysis. Figure 14 summarizes the details of each of the experimental steps.

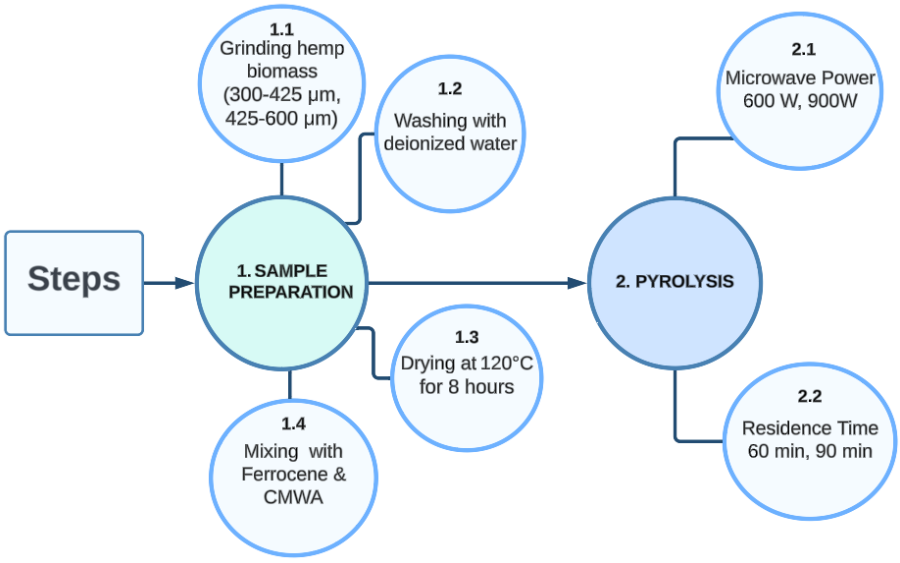

Figure 14: Process flow diagram of the study.

3.3.1 Sample Preparation

Four steps were required for the biomass to be prepared for pyrolysis: grinding, washing, drying, and mixing. First, hemp biomass was ground using a Thomas-Wiley laboratory mill Model 4, and two different particle sizes were separated using an Endecotts Model EVL1 shaker with the following particle sizes, 300-425 µm, and 425-600 µm. After that, the ground hemp of two different sizes was thoroughly washed with deionized water to remove any impurities. Then, it was dried in an electric oven at 120℃ for 8 hours. Lastly, biochar and ferrocene were mixed with the hemp biomass at ratios of 1:10 and 1:5, respectively. The sample weight for each experiment was approximately 65 grams. Specifically, 50 grams of hemp biomass were mixed with 5 grams of previously produced hemp biochar and 10 grams of ferrocene to catalyze the reaction. Biomass is not a good microwave absorber, and when microwaved, it does not reach the appropriate reaction temperatures. Thus, pyrolysis systems employ external microwave absorption materials

often known as carbon microwave absorber (CMWA) [62,63]. Furthermore, by using ferrocene as a catalyst, it is possible to produce GLC material at a much lower temperature [14,15,54].

3.3.2 Microwave Pyrolysis

The Microwave pyrolysis trials were carried out at UNB's Bioenergy Bioproducts Research Lab (BBRL) in accordance with the standard operating procedure and lab manuals. There were two water inputs required to conduct the experiment. These were activated at least thirty minutes before the experiment began to achieve the necessary operating conditions. The microwave generator required a flow of cooling water to circulate through it, ensuring its proper functioning and preventing overheating. This water supply needed to be maintained at a temperature of 20˚C and flow at a rate between four and five liters per minute. A flowmeter was attached to the water tubing to monitor the flow rate. The required temperature and flow rate were achieved through the utilization of a Bradley Navigator Thermostatic Mixing Valve (S19-2000) and a flow regulator, respectively. The second water input was designated for the condenser, but it was not a consideration for this study as it did not focus on bio-oil production.

Following this, the arrangement of the feedstock in the reactor was necessary. The reactor comprised three parts: a bottom piece with a single opening, and a top piece with three openings, the purposes of which will be explained later. Figure 15 depicts an image of the reactor. The middle piece served as the main chamber of the reactor, housing the feedstock. Specially designed clamps connected the middle chamber to the top and bottom sections. A screen was inserted at the interface of the middle and bottom sections to support the

biomass and facilitate the collection of the pyrolyzed product. Once the middle and bottom sections of the reactor were assembled, the feedstock was inserted into the reactor. Subsequently, the reactor was placed into the modified microwave cavity, where the top section of the reactor was connected to the reactor assembly. Three spouts extending from the top section of the reactor passed through the ceiling of the microwave cavity. Two of the reactor openings were necessary for thermocouple insertion, and the third opening was needed for nitrogen purging. The bottom opening of the reactor extended through the floor of the microwave cavity, connecting to the condenser to allow the condensation of volatile gas. Specialized tubing connected to the outlet at the end of the condenser and extended up to a fume hood for the exhaustion of incondensable gases. The entire microwave cavity was covered with steel mesh to prevent microwave radiation leakage during operation. The nitrogen converter was activated and ran for approximately 30 minutes before the experiment to ensure an inert reaction atmosphere. A laptop was connected to the microwave system and the thermocouple to set the power level for the experiment and monitor and record temperature data. Figure 15 shows the microwave system and reactor.

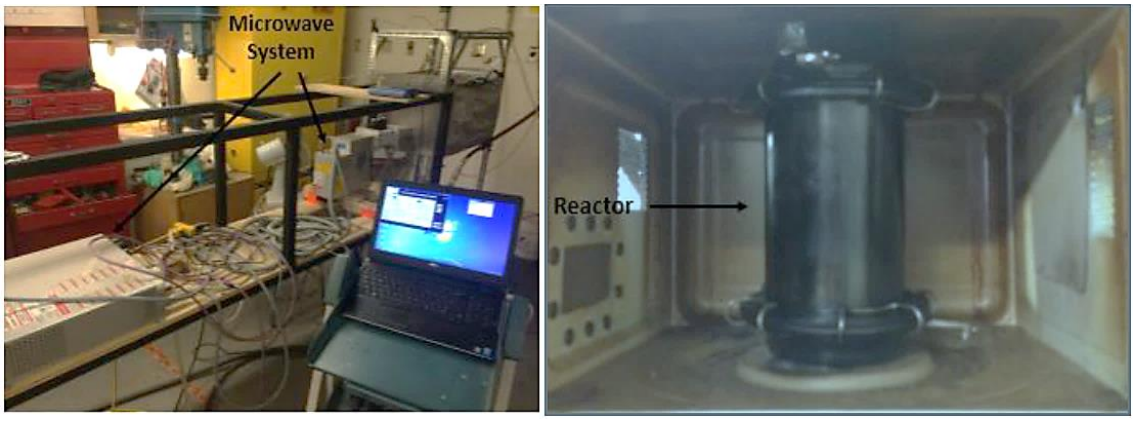

Figure 15: Microwave pyrolysis system and reactor in the UNB Bioenergy and Bioproducts Research Laboratory (BBRL).

Figure 16 displays a schematic of the complete pyrolysis system.

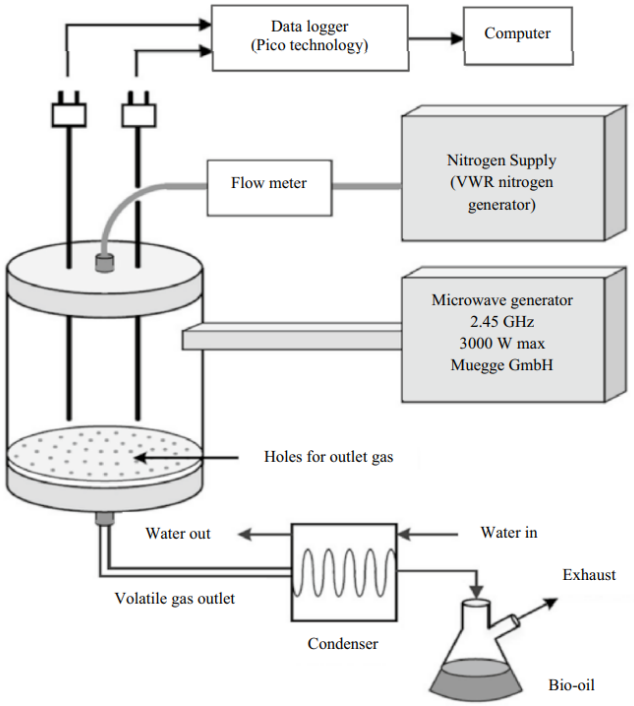

Figure 16: Schematic of the pyrolysis system [2].

This image shows the microwave generator, which operates at a frequency of 2.45 GHz with a maximum output power of 3000 Watts. It also shows the VHR nitrogen generator that is used for producing nitrogen to purge the reactor. A flowmeter is placed in series with the nitrogen supply to measure and ensure a constant nitrogen flow rate. From the top of the reactor, the Pico Technology thermocouple is shown, which connects to the computer for data acquisition. From the bottom of the reactor, the volatile gas outlet is shown extending to the condenser and then to the final exhaust.

Two different residence times were investigated in this study, namely 60 minutes and 90 minutes. Experiments were run at microwave power levels of 20% (600W) and 30% (900W).

It should be stated that the temperature measurement is not completely reliable. Temperature measurement in microwave systems has been frequently documented as a problem area, and significant effort was made in this study to capture the temperature profile as accurately as possible [27,62]. That is why this study employed microwave power as a more dependable metric instead of residence temperature.

3.3.3 Post-Experiment Procedures

First, the microwave power was shut off at the end of the experiment, along with the condenser water. The nitrogen was left running to ensure the material would not combust and would cool down properly. Similarly, microwave water was left running to ensure the microwave system could cool down properly. The cool-down process was allowed to run for approximately 45 minutes to an hour until the thermocouple read in the range of 35˚C – 45˚C. Then, the nitrogen flow was shut off, and the reactor was removed from the microwave system. The pyrolyzed product was removed from the reactor, and the yield was recorded. The temperature profile was saved, and the steady-state temperature reached for the experiment was recorded. Any additional observations on the temperature profile or experiment outputs that seemed notable were also recorded.

3.4 Characterization

Graphene research and study requires a thorough characterization of graphene which includes examining its morphology, characteristics, defects, and layers in detail through spectroscopic and microscopic methods [64]. For this study, the characterization techniques included Raman spectroscopy, x-ray diffraction (XRD) analysis, Fourier-

transform infrared spectroscopy (FTIR) analysis, BET and N_2 adsorption/desorption isotherm analysis, elemental analysis and scanning electron microscopy (SEM) analysis.

3.4.1 Raman Spectroscopy

Raman spectroscopy is an excellent analytical technique used to examine the structure and quality of carbon-based materials. The Raman spectrum of graphene consists of the D peak (1320–1350 cm^{-1}), G peak (1580–1605 cm^{-1}), and 2D or G' peak (2640–2680 cm^{-1}). In relation to the graphite layers, the D mode is linked to any imperfections or disarray, while the G and 2D bands stand for the two-dimensional hexagonal lattice. In certain instances, a D' peak, resulting from defective and double-resonance occurrences, is visible at around 1602-1625 cm^{-1} [65]. A higher defect intensity increases the I_D/I_G ratio; however, the ratio decreases as the carbon structure becomes more amorphous [66]. A high-quality graphene material is indicated by a combination of a low I_D/I_G ratio and a high I_{2D}/I_G ratio being present simultaneously [67]. For example, the D vibration band for GO and rGO can be identified at 1348.31 and 1353.20 cm^{-1}, respectively in Figure 17 (d).

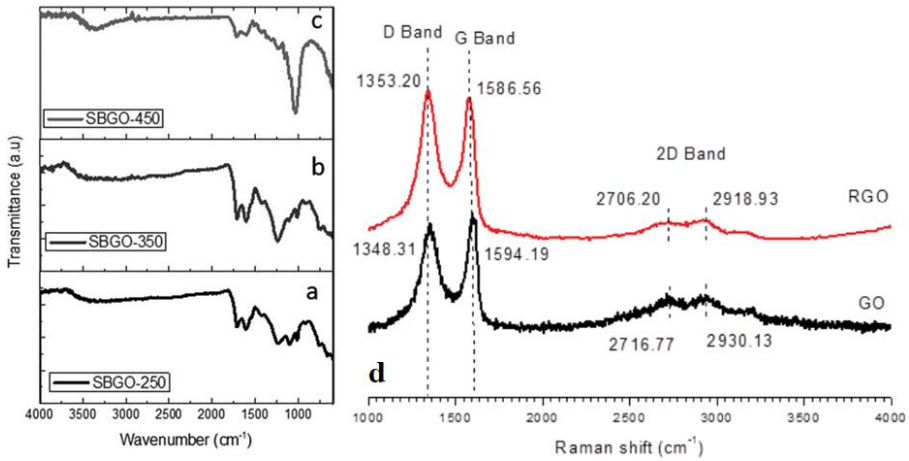

Figure 17: FTIR spectra of GO produced from SB at different temperatures (a) 250 °C (b) 350 °C and (c) 450 °C [11]. And (d) Raman spectra for GO and RGO [68].

The G vibration for GO was observed at 1594.19 cm^{-1} and for rGO at 1586.56 cm^{-1}. Furthermore, the G vibration band is influenced by the stretching C-C bond, which can be found in all sp^2 carbon systems. The 2D band for GO was seen at 2716.77 cm^{-1}, which was shifted to a higher wavenumber and used to identify the layers of graphene. The 2D band was detected at 2706.20 cm^{-1} after reducing GO to rGO. This was accomplished by stacking the graphene layers and removing the oxygen moiety from GO. In addition, the I_D/I_G ratio for GO was 0.86, whereas, in the case of rGO, the I_D/I_G ratio increases as a result of the restoration of sp^2 carbon and the decrease in average sizes of sp^2 domains.

3.4.2 XRD Analysis

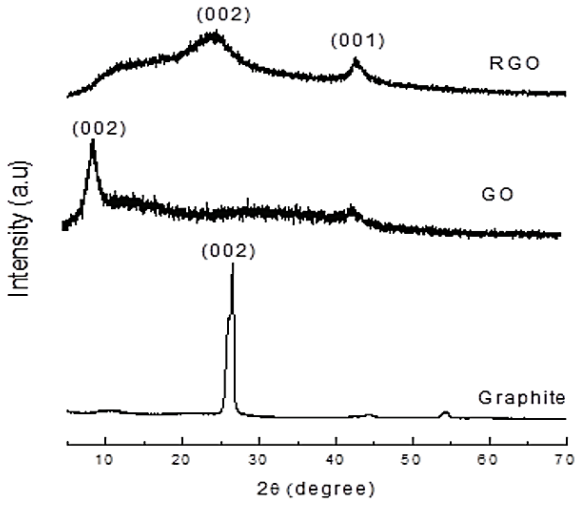

Figure 18: XRD spectra of graphite, GO, and rGO [68].

XRD is an extremely useful non-invasive approach that can be used to analyze the crystalline structure of a material. It can help to identify different structures, phases, and preferred crystal orientations, as well as other structural characteristics like the average grain size, level of crystallinity, strain, and imperfections in the crystal structure [69].

Typically, XRD analysis of pristine graphite and GO produces peaks at 2θ of approximately 26° and 11°, respectively [65]. Hidayah et al. [68] used XRD to study the crystal phase and calculate the interlayer spacing of graphite, GO, and rGO. Figure 18 displays their XRD results.

For graphite, there was a single sharp peak at 2θ = 26.62°. This peak confirmed the presence of an orderly layer arrangement with a d-spacing of 0.3346 nm (FWHM = 0.3456) in the (002) orientation. For GO, the peak was at 2θ = 9.03°, implying that the graphite had been completely oxidized into GO. After eliminating the oxygen-containing functional groups, a broader peak was observed for rGO at 2θ = 24.10°. When compared to graphite, which has a distinct, strong (002) peak in its high crystallization structure, the presence of a wider peak (002) for rGO implies that the (002) crystal phase was not organized in any particular pattern (Figure 18). The creation of one or a few layers of rGO following the reduction from GO may be the reason for the poor organization. Additionally, there was a notable decrease in the d-spacing of rGO from 0.97942 nm to 0.36895 nm, demonstrating the successful removal of oxygen-containing functional groups [68].

3.4.3 FTIR Analysis

FTIR can be used to detect the presence of diverse functional groups and can be utilized to evaluate and categorize the chemical structures of the sample that have been heated. GO contains a lot of oxygen functional groups and chemical modifications can cause alterations in these groups, so FTIR could be a beneficial tool in looking at the composition of GO and any changes in the structure due to modifications. Figure 17 (a-c) illustrates the FTIR spectra of GO synthesized from sugarcane bagasse at various temperatures. Analysis of

Figure 17 of the FTIR showed that the C = O stretching frequency at 1715 cm^{-1} was present at all three temperatures, indicating the presence of a carbonyl group following pyrolysis. Notably, this peak was most prominent at 350° C. Furthermore, the aromatization and condensation of non-graphitic glucose monomers were confirmed by the C = C stretching at 1604 cm^{-1} that appeared at all temperatures, with the peak being particularly sharp at the same temperature. Additionally, the peaks of the epoxy and C–O–C groups were observed at 1026 cm^{-1} and 1243 cm^{-1}, respectively, at all times, with the peak being especially strong at 450° C due to the increased formation of epoxy groups as the sample was heated [11].

3.4.4 BET and N_2 Adsorption/Desorption Isotherm Analysis

An analysis of the synthesized material's surface features was conducted using the Brunauer, Emmett, and Teller (BET) method. In this method, nitrogen was used as an absorbent during the physisorption process, yielding data such as specific surface area (m^2/g), porosity distribution (cc/g), and average pore size (Å).

3.4.5 Elemental Analysis

The elemental analysis of synthesized samples was performed using a Perkin Elmer 2400 CHNS/O Series II elemental analyzer at the Limerick Pulp and Paper Center, University of New Brunswick. The elemental analysis was conducted to assess the impact of process parameters, including microwave power, residence time, and feedstock particle size, on the elemental composition of synthesized materials. Moreover, the H/C ratio could also be determined from this test, which was used as an indicator of the aromatic characteristics and stability of the pyrolyzed samples.

3.4.6 Scanning Electron Microscopy Analysis

SEM is often a convenient way to analyze the morphology and structure of graphene-based materials. Its benefits include being able to observe contaminants, wrinkles in graphene, and discontinuities that may occur during synthesis. Still, it is limited in its ability to decipher ultra-thin layers of graphene [64]. In addition, energy dispersive spectrometry (EDS) in conjunction with a field emission scanning electron microscope (FE-SEM) is typically used to analyze an element's composition**.**

Chapter 4

Results and Discussion

4.1 Heating Performance and Yields

Table 5 presents data on microwave pyrolysis temperatures and product yields. In this investigation, the heating rate (℃/min) was defined as the temperature increase within the initial ten minutes of the experiment, while the residence temperature (℃) was determined as the average temperature during the latter half of the experiment.

Table 5: Microwave pyrolysis temperature data and product yield.

Sample	MW Power (W)	Particle Size (µm)	Residence Time (min)	Heating Rate (℃/min)	Residence Temperature (℃)	GLC Yield (wt.%)
30 H 60	900 (30%)	425-600 (H)	60	53.5 ± 13.46	851 ± 66	4.46 ± 0.87
30 H 90			90		864 ± 17	2.54 ± 0.10
30 L 60		300-425 (L)	60	44.16 ± 13.88	816 ± 34	5.92 ± 0.11
30 L 90			90		860 ± 30	2.92 ± 0.41
20 H 60	600 (20%)	425-600 (H)	60	33.8 ± 13.05	791 ± 25	7.54 ± 0.40
20 H 90			90		800 ± 25	3.62 ± 0.76
20 L 60		300-425 (L)	60	28.08 ± 10.46	796 ± 37	8 ± 0.21
20 L 90			90		757 ± 11	5.15 ± 0.33

At the sample designation "30 H 60," the numeral 30 denotes the microwave power level, the letter H signifies the feedstock particle size, and the numeral 60 indicates the residence time. Table 5 indicates that the residence temperature fluctuated between 800-860 ℃ throughout all the experiments. Given the limited reliability of temperature measurements using a thermocouple in microwave pyrolysis, this study will employ microwave power as a more dependable metric instead of residence temperature.

The sample generated with 30% microwave power and larger particle size exhibited the highest heating rate, reaching approximately 53 ℃/min. Conversely, the samples produced with 20% microwave power and smaller particle size displayed the lowest heating rate, measuring around 28 ℃/min. Notably, a discernible trend emerged wherein the heating rate diminished with a decrease in both microwave power level and feedstock particle size.

Conventionally, a reduction in feedstock particle size tends to elevate the heating rate due to increased external surface area and enhanced contact with susceptors. However, an intriguing finding from a separate study [19] indicated that reducing the particle size to a specific threshold (e.g., less than 0.25 mm) led to a decline in the heating rate. This phenomenon could be attributed to the higher ash content associated with smaller particle sizes, impeding effective heat transfer.

In Figure 19, the bar chart illustrates the GLC yield per sample. The sample with the highest yield, approximately 8 wt.% (around ~5.2 grams out of 65 grams of initial feedstock), was obtained using 20% microwave power, a smaller particle size, and a residence time of 60 minutes (labeled as 20L60). Conversely, the lowest yield, around 2.5 wt.% (around ~1.6 grams out of 65 grams of initial feedstock), was observed for the sample produced with

30% microwave power, a larger particle size, and a 90-minute residence time (labeled as 30H90).

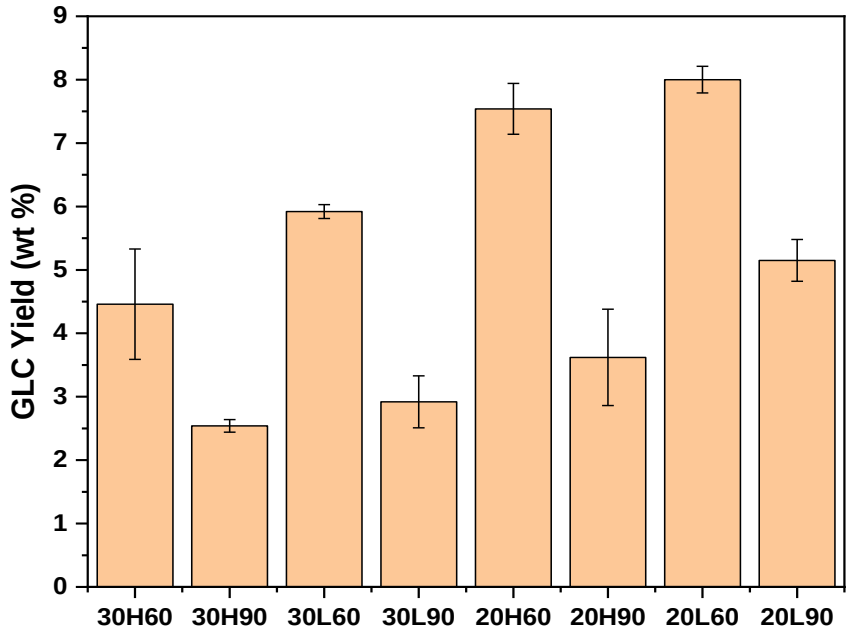

Figure 19: GLC yield per sample.

The study revealed that reducing microwave power level and feedstock particle size correlates with an increase in GLC yield. This phenomenon is attributed to the lower heating rate associated with both lower microwave power levels and smaller feedstock particle sizes [41]. Elevated heating rates were generally found to facilitate the cracking of organic components in feedstock and the condensation of volatiles into gaseous products [70]. As a result, the GLC yield demonstrates an increase under conditions of lower heating rates. Furthermore, it was observed that GLC yield decreases with extended residence time. Prolonged residence periods afford more time for the interaction between reactants in the volatiles and the char, ultimately leading to a higher gas yield [26]. This elucidates the reason for the observed reduction in GLC yield with prolonged residence time.

4.2 Raman Spectroscopy

In accordance with ISO/TS 21356-1:2021 [71], a preliminary Raman spectroscopy analysis is recommended before engaging in detailed characterization techniques. This preliminary step aims to ascertain the presence of graphene or graphitic material in the samples, as it represents the most efficient approach for promptly and easily characterizing their structure and quality. Graphene, or functionalized graphene produces distinct peaks at specific wavelengths during Raman spectroscopy. The identification of materials and their quality is achievable through the analysis of peak locations and intensities.

In this investigation, Raman analysis was executed using a Reinshaw inVia Raman Microscope, employing a He–Ne laser with a wavelength of 633 nm. The spectral range was recorded within the wavelength range of 500 to 3000 cm^{-1}. Measurements were conducted on three replicate samples, each assessed at three different points.

The identification of graphene in a sample relies on the observation of three distinct peaks: the D-band, G-band, and 2D band[72]. However, the presence of functionalized graphene or GO alters the Raman spectroscopy results, displaying the D and G peaks without necessarily displaying a 2D peak [71]. Synthesized samples in this study displayed prominent peaks around 1325 cm^{-1} and 1590 cm^{-1}, as illustrated in Figure 20.

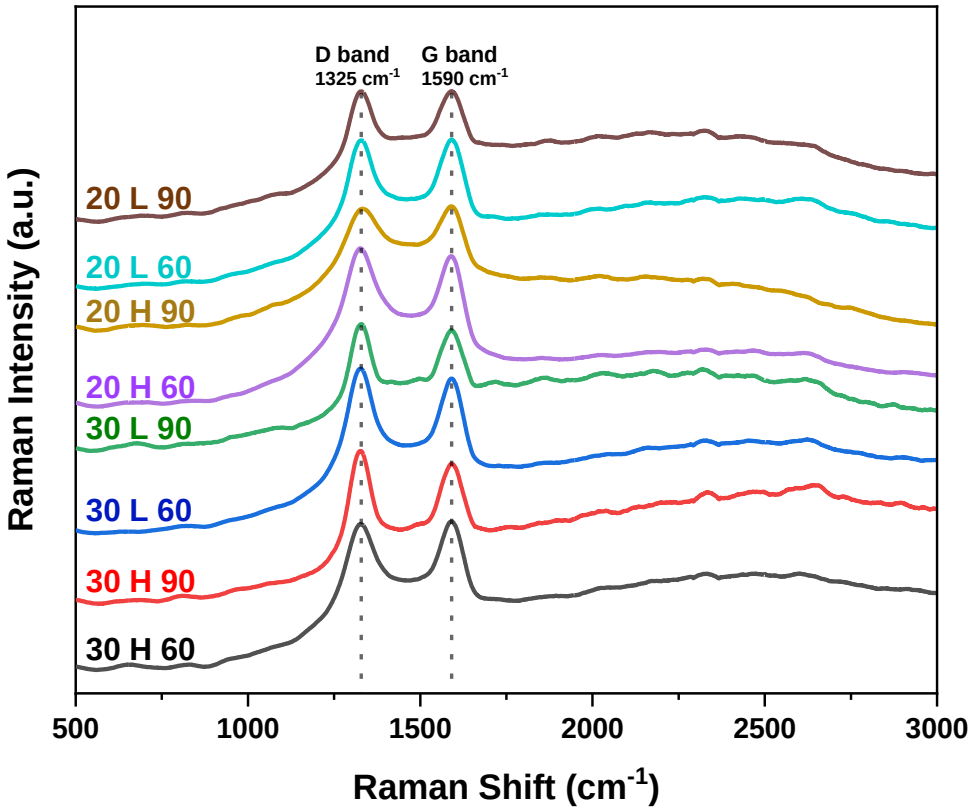

Figure 20: Raman Spectra of the synthesized samples.

In this context, the presence of the D band, detected around 1325 cm^{-1}, signified the existence of imperfections or distorted sp^2 carbon bonds, indicating lattice irregularities stemming from disordered sp^3 carbon atoms and the existence of oxygen within the structure. Conversely, the appearance of the G band around 1590 cm^{-1} served as the first-order Raman band for all sp^2-hybridized carbon, specifically linked to a distinct vibrational mode termed E_{2g}, prevalent in both ring and chain configurations [73–75]. The ratio between the D band and G band, denoted as I_D/I_G, serves as an indicator of the disorder or defects present in the produced material.

The I_D/I_G ratios corresponding to various synthesized samples are provided in Table 6.

Table 6: I_D/I_G ratio of different samples.

Sample	I_D/I_G
30H60	0.99 ± 0.07
30H90	1.07 ± 0.03
30L60	1.05 ± 0.03
30L90	1.03 ± 0.02
20H60	1.05 ± 0.08
20H90	0.99 ± 0.03
20L60	1.04 ± 0.04
20L90	1 ± 0.07

The outcomes from Raman spectroscopy and the I_D/I_G ratio initially suggested that the synthesized material might be GO, aligning with earlier research [73,76]. This assertion was further validated by corroborative evidence from XRD and FTIR analysis.

4.3 XRD Analysis

X-ray diffraction (XRD) patterns were captured using a Bruker D8 Advance X-ray diffractometer (40 kV, 40 mA, Cu Kα radiation, $\lambda = 1.5418$ Å) at room temperature. The data collection spanned the range of $5° < 2\theta < 80°$, employing a scan rate of 2° min^{-1} and a step width of 0.02°.

The X-ray diffraction patterns of the as-prepared samples are depicted in Figure 21 below. All the samples displayed a diffraction peak at approximately $2\theta \approx 13.3 – 13.5°$, indicating

an interplanar spacing of around ~0.65 − 0.66 nm, confirming the successful synthesis of GO in each sample [77,78].

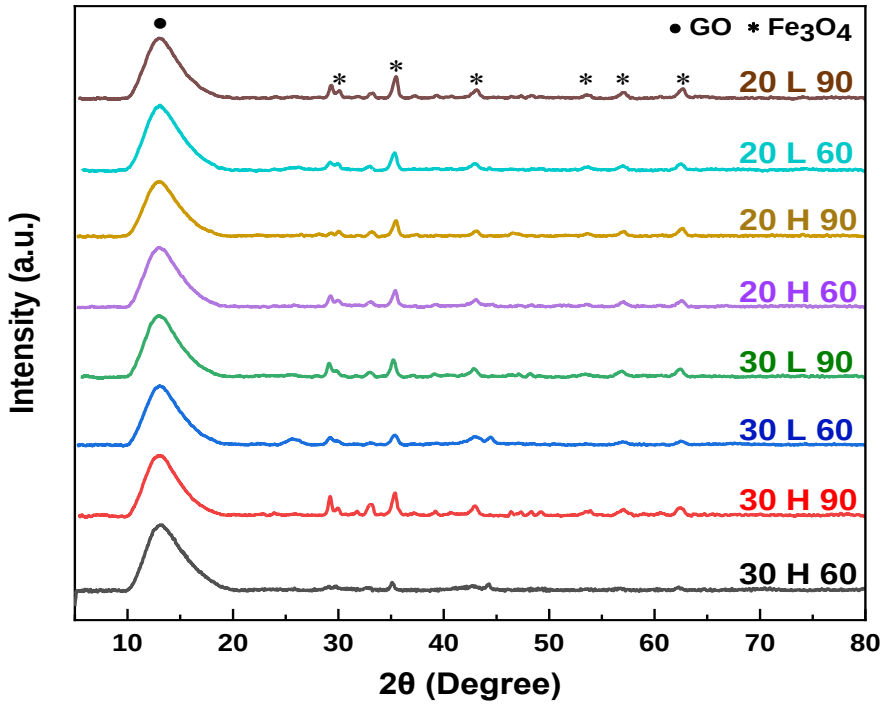

Figure 21: XRD spectrum of the synthesized samples.

The interplanar distance of GO varied with the amount of absorbed water molecules, ranging from 0.61 nm for "dry" GO (2θ ≅ 13° − 14°) to 1.2 nm for "hydrated" GO (2θ ≅ 8° − 9°) [77]. Consequently, the higher value of 2θ in this study suggests that the synthesized samples are indeed dry GO.

In Figure 21, several additional peaks are evident at approximately 30°, 35.4°, 43°, 53.6°, 56.9°, and 62.5°, corresponding to Fe_3O_4 (iron oxide) (JCPDS, 19-0629). For samples 30H60 and 30L60, an additional peak at 44° was observed which corresponds to Fe-C (iron carbide) [79]. The presence of these oxide and carbide particles signifies impurities in the samples, and these can be removed using sulfonation process [80]. Another minor peak

around 2θ = 33° is discernible, possibly attributable to the presence of Ca or Si in the samples [81,82]. Table 7 presents the values for the interlayer spacing (d), crystallite size, and the number of layers in the samples.

Table 7: Comparison of structural parameters of the samples resulting from the XRD patterns.

Sample	Peak (2θ)	d-spacing (nm)	Crystallite Size (nm)	Number of Layers
30H60	13.591	0.651	1.90	2.53
30H90	13.325	0.664	2.10	2.76
30L60	13.419	0.659	2.05	2.70
30L90	13.334	0.664	2.10	2.75
20H60	13.368	0.662	2.09	2.74
20H90	13.314	0.664	2.11	2.76
20L60	13.439	0.658	1.99	2.62
20L90	13.366	0.662	2.10	2.75

The interlayer spacing was determined utilizing Bragg's law of X-ray diffraction [83], as described in equation 1.

$$n\lambda = 2d\ sin\theta \quad [1]$$

In the aforementioned equation, θ represents the diffraction angle, n denotes the degree of diffraction (considered as unity), λ stands for the wavelength of the Cu Kα radiation (0.15406 nm), and d represents the interplanar spacing. In this context, the diffraction peak corresponding to GO at 2θ ≈ 13.3 – 13.5° was employed to compute the interlayer spacing.

The crystal size (C), associated with the stacking of graphene layers, was determined using the Scherrer equation [83]. This calculation involved utilizing the Full Width at Half Maximum (FWHM) values of the GO diffraction peak, as described in equation 2.

$$C = \frac{0.89\lambda}{\beta.cos\theta} \quad [2]$$

In this context, λ represents the wavelength used, β is the line width at half height in radians, and θ is the diffraction angle. The determination of the number of graphene layers involved dividing the crystal size (C) by the interlayer distance (d) and adding the thickness of an atomic layer [83], denoted as "a" (0.1 nm), as articulated in equation 3.

$$n = \frac{C}{d+a} \quad [3]$$

Table 7 reveals a noteworthy trend: both the d-spacing and crystallite size of the samples exhibit an increase with prolonged residence time. This phenomenon can be linked to the destruction of micropores or the blockage of pores over time, as evidenced by the physisorption analysis data. The extended residence time leads to pore blockage, trapping volatiles generated during pyrolysis inside, causing condensation. This entrapment of volatiles serves as the underlying cause for the escalating d-spacing and crystallite size during extended residence periods. These observations align consistently with the findings from the FTIR analysis.

It was noted that, with a residence time of 90 minutes, neither microwave power nor particle size exerted a noteworthy influence on the d-spacing or crystallite size of the samples. However, in other cases involving variations in microwave power or particle size, the consistent pattern observed is that samples with lower porosity exhibit greater d-spacing and crystallite size. This phenomenon can be attributed to the heightened release

of volatiles in samples with high porosity, leading to a reduction in d-spacing and crystallite size.

The number of layers in the samples were determined using Equation 3. According to the data presented in Table 7, it can be concluded that the synthesized GO in each sample comprises 2-3 layers.

4.4 FTIR Analysis

FT-IR spectra were acquired on the Thermo Fisher Nicolet 6700 FT-IR spectrometer. The wavenumber region and resolution were 4000–400 cm^{-1} and 0.5 cm^{-1}, respectively, and 32 scans were acquired for each measurement. The samples were prepared in KBr tablets. Briefly, ~1 mg of each measured sample was mixed in a mortar with 400 mg of KBr and next pressed in a hydraulic press to form a solid tablet.

Figure 22 illustrates the Fourier-transform infrared (FT-IR) spectra of untreated hemp biomass.

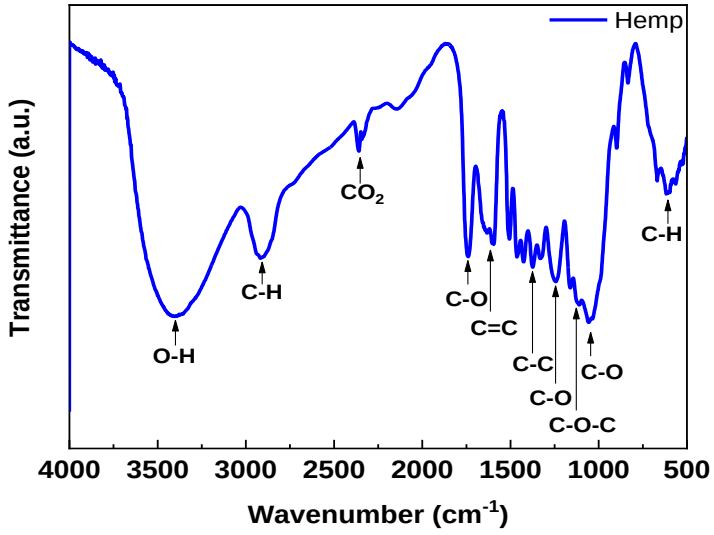

Figure 22: FTIR spectra of raw hemp biomass.

The significant peak spanning from 3600 to 3200 cm^{-1} is attributed to O–H stretching, a distinctive feature of crystalline cellulose. Aliphatic and aromatic compounds are associated with C–H stretching observed in the ranges of 2850–2890 cm^{-1} and 700–800 cm^{-1}, respectively. Carbon dioxide (O=C=O) is detected at approximately 2400 cm^{-1}. The vibration at 1735 cm^{-1} corresponds to the C=O peak, indicative of carboxylic acids in hemicellulose. The characteristic C=C stretching for cellulose compounds is observed in the range of 1600 to 1740 cm^{-1}. A stretch indicative of C–C aromatic rings is evident around 1435–1475 cm^{-1}. Notable C–O stretching, and deformation are observed at 1215 and 1060 cm^{-1}, respectively, while the stretching vibration near 1160 cm^{-1}, attributed to the C–O–C functional group, is associated with lignin [2].

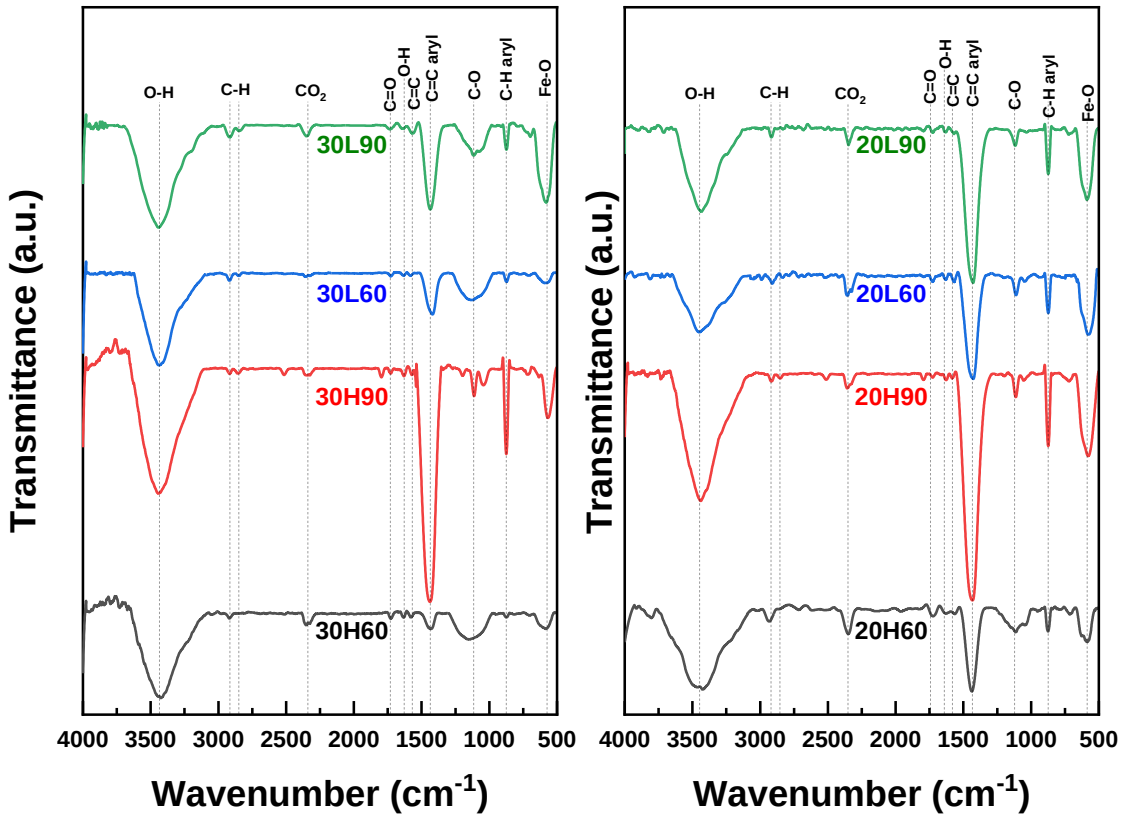

Figure 23: FTIR spectra of as synthesized samples.

Figure 23 represents the FTIR spectra of synthesized samples. By comparing it to the raw spectra it can be said that after pyrolysis most of the bands got reduced significantly or disappeared and some new bands were formed.

Graphene oxide is composed of sp^3-hybridized carbons (with hydroxyl and ether/epoxy functional groups arranged on the top and bottom of the surfaces) and sp^2-hybridized carbons (with carbonyl and carboxyl functional groups in the sheet and on the edges). Between the GO layers, hydrogen bonds may appear [84]. We avoid discussing the bands from the fingerprint region, since definitive assignment of these bands for such a complex material as GO is difficult [85].

Figure 23 illustrates a prominent and broad peak, centered between 3405-3436 cm^{-1}, attributed to O-H stretching vibrations of the C–OH groups, H_2O and carboxylic acids [86]. The peaks at 2845-2865 cm^{-1} and 2911-2932 cm^{-1} are assigned to the symmetric and asymmetric stretching of residual CH_x groups, respectively [87]. Notably, the peak centered at 2338-2353 cm^{-1} is indicative of CO_2 intercalation between the GO planes [86]. Additionally, the peak at 1724-1729 cm^{-1} is attributed to C=O stretch modes associated with carbonyl and carboxyl groups [88]. The peak at 1627-1633 cm^{-1} is assigned to O-H vibrations of adsorbed water, with a divergence in interpretations among researchers regarding its association with the C=C bond or water bending modes [89]

Furthermore, the peak centered at 1570-1582 cm^{-1} is linked to C═C stretching of sp^2 hybridized carbons [86]. while the band at 1428-1444 cm^{-1} is indicative of C=C stretching in aromatic ring structures [87]. A distinct peak in the range of 1107-1140 cm^{-1} corresponds to the stretching vibration of the C-O group in epoxy structures [90]. The characteristic feature at 872-875 cm^{-1} signifies aromatic C-H out-of-plane bending [87]. Lastly, the band

centered around 565-595 cm^{-1} is associated with the Fe─O stretching mode characteristic of Fe_3O_4 [91].

Through FTIR analysis, the presence of the aforementioned functional groups suggests that GO has been successfully synthesized. The FTIR spectrum of the GO sample aligns closely with previous research. Confirmation of the successful synthesis of GO is supported by the results obtained from XRD and Raman Spectroscopy, and this confirmation is reinforced by the subsequent FTIR analysis.

From Figure 23, it was observed that any change in residence time, microwave power, or feedstock particle size does not have any significant effect on the FTIR bands except for the O-H, aryl C=C, aryl C-H, and Fe-O band.

The band centered between 3405-3436 cm^{-1} which arises due to the O–H-vibrations of the C–OH-groups, H_2O, and carboxylic acids was observed to follow the general trend that the sample with less porosity shows an intense O-H peak. This might be attributed to the condensation of entrapped volatile due to the pore-blocking effect present in the less porous samples. This observation is also in accordance with the XRD results.

The intensities of aryl C=C, and aryl C-H peaks exhibit an inverse correlation with the microwave power levels. A reduction in power level results in increased intensity of these peaks; however, this effect is less pronounced in samples subjected to prolonged residence time. This behavior can be attributed to the diminished heating rate associated with the reduced microwave power level. Slower heating rates afford an extended timeframe for the carbonization process, fostering the development of more orderly and aromatic carbon structures [87,92]. This is why with a decrease in the microwave power level the intensities of aryl C=C, and aryl C-H peaks get intensified. The Fe-O band was also observed to follow

the same relationship with the microwave power level. Lower heating rate was found to be more favorable for the formation of magnetite.

In contrast, an increase in residence time was observed to result in higher intensities of aryl C=C, aryl C-H, and Fe-O peaks. This phenomenon can be attributed to longer residence times enabling more extensive carbonization, thereby promoting the formation of aromatic structures from the carbon precursors [70,93].

The impact of feedstock particle size on the intensities of aryl C=C and aryl C-H peaks presents an intriguing observation. It was noted that the intensity of these peaks rises with a decrease in feedstock particle size, specifically within the 60-minute residence time. This trend can be attributed to the lower heating rate associated with smaller feedstock particles. However, when the residence time extends to 90 minutes, a reversal is observed, wherein the aryl C=C and aryl C-H peaks are more pronounced with larger feedstock particle sizes. The lower heating rate, conducive to aromatization, may suggest that for the 90-minute residence time, samples with smaller particle sizes reach a plateau or experience a decline as they undergo further transformation. Conversely, samples with larger particle sizes continue to exhibit an increase in intensity over prolonged residence times. This could explain the heightened aryl C=C and aryl C-H peaks in larger-size particle samples compared to smaller ones after 90 minutes of residence time.

4.5 BET and N_2 Adsorption/Desorption Isotherm Analysis

Nitrogen adsorption/desorption isotherms of the samples were measured at 77 K using a BELSORP-max (MicrotracBEL Corp.) to determine the surface areas and total pore volumes. Prior to measurement, samples were outgassed at 200°C under nitrogen flow

overnight. The surface areas, S_{BET}, were calculated using the Brunauer–Emmett–Teller (BET) equation, which is the most widely used model for determining the specific surface area. A part of the nitrogen adsorption isotherm in the P/P_0 range 0.10–0.30 was fitted to the BET equation to estimate the S_{BET}. The total pore volumes, V_{total}, were calculated based on the amount of nitrogen adsorbed at $P/P_0 = 0.99$.

In addition, the micropore volume and external surface area (mesoporous surface area) were calculated from the adsorption branch of the isotherm using the *t*-plot method. The micropore surface areas were obtained by subtracting the mesopore surface area from the corresponding BET surface area, and the mesopore volume was obtained by deducting the micropore volume from the total pore volume [94].

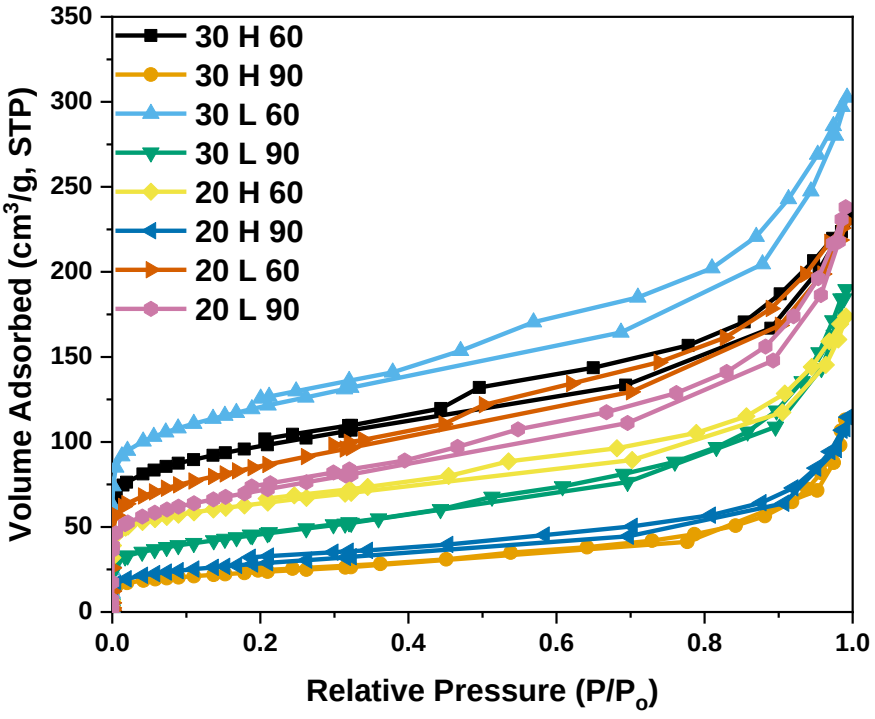

Figure 24: Nitrogen adsorption-desorption isotherms of the samples at 77 K.

According to the International Union of Pure and Applied Chemistry (IUPAC) pore dimension classifications, the pore of a porous absorbent is grouped into micropores (pore width <2 nm), mesopores (2–50 nm), and macropores (>50 nm) [95]. The N_2 adsorption/desorption isotherms of the samples are shown in Figure 24. The detailed pore structure parameters of the samples are listed in Table 8.

According to Figure 24, all of the nitrogen adsorption/desorption isotherms were of a combined type I and type IV isotherm with a hysteresis loop of type H4. The hybrid Type I–IV isotherms with H4 hysteresis is characteristic of solid porous materials having both microporous and mesoporous structures [96]. The initial part of the isotherms is of Type I, indicative of microporosity, hysteresis loop of the isotherms is of Type IV, indicative of mesoporosity. Moreover, the H4 hysteresis loop is mainly found in solids with slit pores [97].

Table 8: Surface areas and pore volumes of as prepared samples.

Sample	S_{BET} (m^2/g)	S_{meso} (m^2/g)	S_{micro} (m^2/g)	V_{total} (cm^3/g)	V_{meso} (cm^3/g)	V_{micro} (cm^3/g)	D_p (nm)
30H60	346.61	91.02	255.59	0.35	0.21	0.15	4.10
30H90	82.22	29.66	52.55	0.17	0.12	0.06	8.49
30L60	423.22	112.91	310.31	0.46	0.27	0.19	4.37
30L90	160.28	95.82	64.46	0.29	0.24	0.05	7.25
20H60	225.90	81.96	143.94	0.27	0.19	0.07	4.73
20H90	97.96	62.45	35.51	0.17	0.15	0.02	6.80
20L60	299.96	90.64	209.32	0.35	0.21	0.14	4.67
20L90	251.64	102.81	148.83	0.37	0.26	0.10	5.82

From Table 8 it was observed that the highest surface area as well as the total pore volume was observed with the lower size particle with 30% microwave power and 60 minutes of residence time. The lowest was observed for the higher size particle with 30% microwave power and 90 minutes of residence time. Figure 25 shows the variation of surface area and total pore volume with different samples.

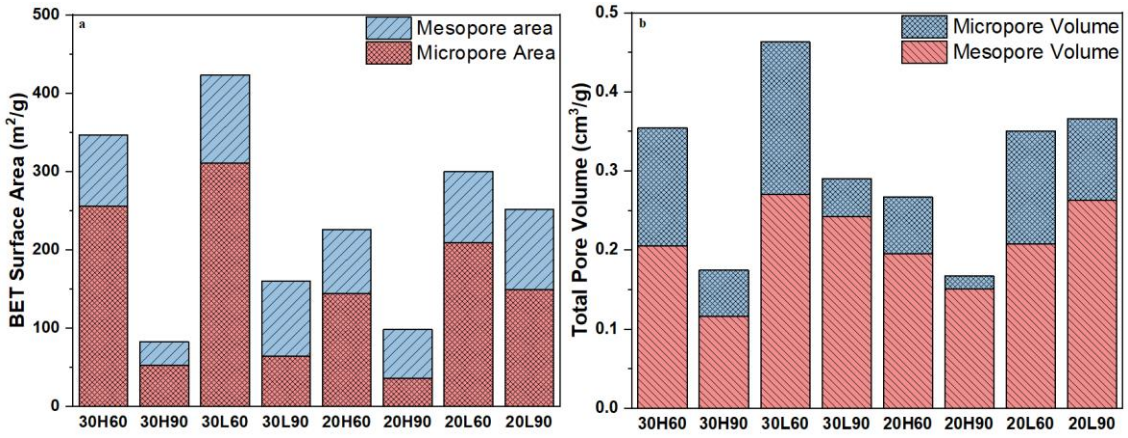

Figure 25: a) BET surface area, and b) Total pore volume of synthesized samples.

It was observed that with the increase in residence time, BET surface area as well as micropore and mesopore surface area decreases in the samples. This might be attributed to the softening of some volatile fractions and the formation of intermediate melt which closes and seals off some of the pores upon increasing the hold time [98–100]. This is also evident from Figure 25 (b) where we observed that with the increase in residence time, the micropore volume decreased significantly which resulted in reduced surface area. The total pore volume also follows a similar trend with residence time as BET surface area except for the samples produced with 20% microwave power and lower size particles (20L60, 20L90). The reason behind this might be attributed to the lower heating rate. As the heating

rate in these samples was the lowest so with prolonged residence time the micropore volume decreased but the mesopore volume was still increasing which resulted in a higher total pore volume.

The effect of feedstock particle size on the BET surface area and total pore volume follows the general trend that when the particle size was reduced the BET surface area as well as the total pore volume increased. This might be attributed to the better micropore properties and lower temperature gradients with smaller particles that would improve the release of volatiles [101]. On the contrary, the BET surface area and the total pore volume increased with an increase in microwave power for 60 minutes of residence time, and it shows the opposite trend for 90 minutes of residence time. This is because a rise in microwave power allows more volatiles of the biomass to evaporate and thus develop more pores which resulted in increases in BET surface area and total pore volume [102]. But with prolonged residence time formation of intermediate melt and pore blocking is more pronounced with higher microwave power. That is the reason why BET surface area and total pore volume decrease with increased microwave power at 90 minutes of residence time.

4.6 Elemental Analysis

To determine the elemental composition of the synthesized materials, an elemental analysis was conducted using a Perkin Elmer 2400 CHNS/O Series II elemental analyzer at the Limerick Pulp and Paper Center, University of New Brunswick.

Table 9 displays the carbon, hydrogen, nitrogen, and sulfur contents.

Table 9: Elemental analysis of individual GLC material sample.

Sample	C (wt. %)	H (wt. %)	N (wt. %)	S (wt. %)	H/C ratio
30H60	73.1	0.7	0.4	1	0.11
30H90	19.5	0.2	0.2	0.2	0.12
30L60	70.9	0.3	0.4	0.1	0.05
30L90	32.5	0.2	0.2	0	0.07
20H60	53.3	0.7	0.4	0.4	0.16
20H90	27.7	0.2	0.3	0.1	0.09
20L60	51.6	0.2	0.4	0.1	0.05
20L90	41.5	0.2	0.3	0	0.06

The process parameters had a notable impact on the carbon and hydrogen content, whereas the changes in sulfur and nitrogen contents due to these factors were relatively minor. Observations revealed that the carbon content tended to rise with an increase in microwave power level for samples produced with a 60-minute residence time, due to heightened carbonization and consequent reductions in oxygen and hydrogen levels [103]. Conversely, the opposite trend was noted for samples produced with a 90-minute residence time, attributed to significant carbon loss through gas-forming reactions over an extended period [104]. Meanwhile, the hydrogen content remained relatively constant with changes in microwave power.

The impact of residence time was more pronounced on the carbon content of synthesized materials, demonstrating a decline with prolonged residence time. This reduction in carbon

and oxygen levels in graphene oxide (GO) samples primarily occurred through the volatilization of elements such as CO, CO_2, H_2O, and hydrocarbons during pyrolysis [105]. Hydrogen content also decreased with residence time for the same reason. This observation indicates that a residence time of 90 minutes was not suitable for the production of GO.

Furthermore, it was observed that carbon content increased with an increase in feedstock particle size for samples produced with a 60-minute residence time. Larger particle sizes favored the devolatilization process, leading to an improvement in carbon content [26]. Conversely, the opposite was observed for samples produced with a 90-minute residence time due to gas-forming reactions. Hydrogen content also increased with particle size for the 60-minute residence time, attributable to lower porosity in samples produced with larger particles. However, for the 90-minute residence time, no effect of particle size was observed on hydrogen content.

Additionally, all the samples exhibit H/C ratios below 0.16, indicating the aromatic characteristics of the produced samples. The H/C ratio serves as an indicator of the aromaticity and stability of the pyrolyzed samples. The decrease in H/C ratio is attributed to the decomposition of oxygen-containing functional groups, including carboxyl, carbonyl, and methoxyl, leading to the formation of aromatic compounds [105].

4.7 Scanning Electron Microscopy Analysis

Figure 26 presents SEM images of the synthesized samples.

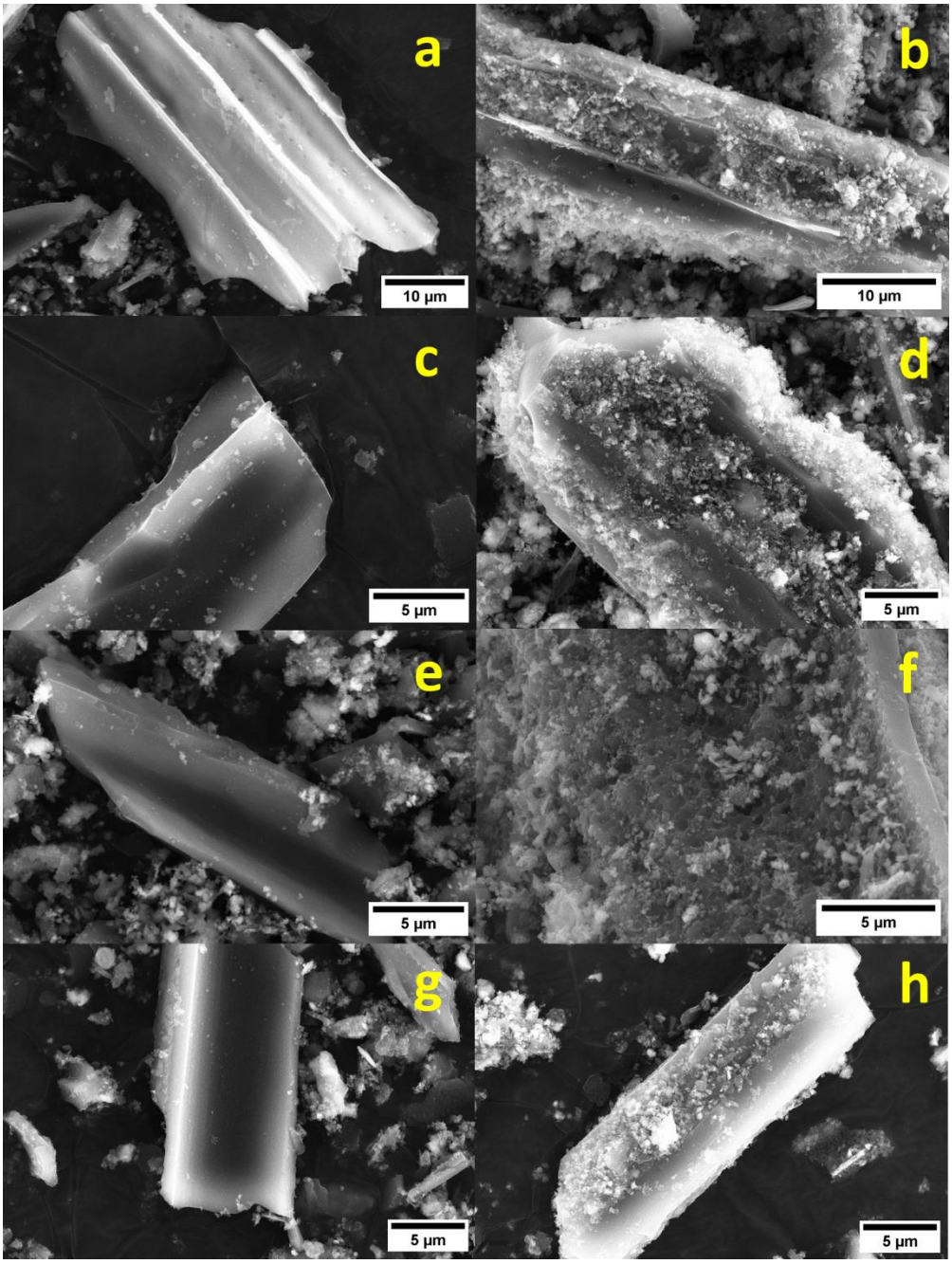

Figure 26: SEM images of synthesized samples a) 30H60, b) 30H90, c) 30L60, d) 30L90, e) 20H60, f) 20H90, g) 20L60, and h) 20L90.

The surface morphologies of the synthesized samples were examined utilizing the high-resolution SCIOS 2 FESEM microscope at the Microscopy and Microanalysis Facility (MMF) of the University of New Brunswick (UNB). The SEM images, as depicted in Figure 26, intricately unveiled the distinctive sheet-like architecture inherent in the synthesized samples. This characteristic structure is a well-established attribute of GO, resulting from the incorporation of oxygen-containing functional groups at the edges of the material [73].

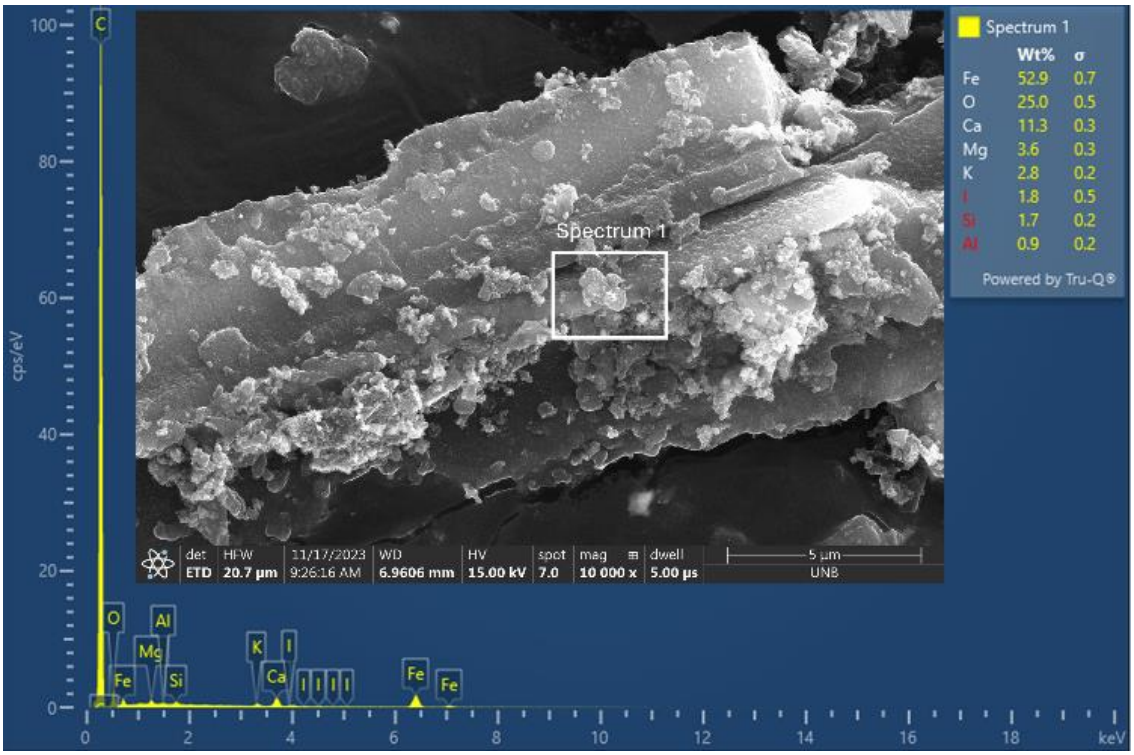

Figure 27: EDS spectrum analysis of GO sample (30H90).

Upon closer examination of SEM images, it became evident that samples subjected to a 60-minute residence time displayed a remarkably smooth surface (Figure 26 (a, c)), and those produced at lower microwave power levels during the same residence time exhibited

even smoother surfaces (Figure 26 (e, g)). However, a discernible presence of impurities, predominantly iron oxide/carbide stemming from the utilization of ferrocene, as well as other minerals (such as Ca, Mg, K), was apparent on the surface. This confirmation is substantiated through Energy Dispersive X-ray Spectroscopy (EDS), as illustrated in Figure 27.

In contrast, samples subjected to a 90-minute residence time revealed a surface characterized by roughness and a multitude of irregularities. These irregularities were postulated to arise from the presence of various functional groups or other impurities within the sample [106]. Furthermore, Figure 26 (f) highlights that a substantial portion of pores were obstructed, attributed to the condensation of intermediate volatiles leading to pore blockage.

Chapter 5

Conclusions and Recommendations

5.1 Conclusions

In conclusion, the comprehensive investigation into microwave pyrolysis of waste hemp biomass for the synthesis of GLC materials has provided valuable insights into the interplay of process parameters and their impact on the resulting materials. The key findings can be summarized as follows:

- The analysis of heating performance and yields unveiled a correlation among microwave power, particle size, residence time, and GLC yield. Notably, lower microwave power levels and smaller feedstock particle sizes were found to correlate with increased GLC yield. This was attributed to the lower heating rates under these conditions, which, unlike higher heating rates, are less conducive to facilitating the cracking of organic components in feedstock and the condensation of volatiles into gaseous products. In contrast, prolonged residence times exhibited a diminishing effect on GLC yield, as increased interaction between reactants and char led to a higher gas yield.

- Raman spectroscopy, XRD analysis, and FTIR analysis collectively confirmed the successful synthesis of GO in the samples. The I_D/I_G ratio from Raman spectroscopy indicated the presence of defects and disorder in the synthesized material.
- XRD patterns displayed distinctive peaks, confirming the presence of GO along with some impurities. An increase in interplanar distance and crystallite size was

observed with prolonged residence time, suggesting the impact of pore blockage and condensation of volatiles. Notably, microwave power and particle size had minimal influence on these parameters, typically showing that samples with lower porosity had larger d-spacing and crystallite size. The number of layers in all samples was found to be in the range of 2-3 layers.

- FTIR spectra indicated the presence of functional groups associated with GO. The FTIR spectrum was in line with prior research, and variations in residence time, microwave power, or feedstock particle size had minimal impact on FTIR bands, except for O-H, aryl C=C, aryl C-H, and Fe-O bands. Notably, the O-H band intensity was affected by porosity, providing insights into pore-blocking effects, consistent with XRD results. Aryl C=C and aryl C-H peaks showed an inverse correlation with microwave power, resulting in intensified peaks at lower power levels. Conversely, increased residence time enhanced these peaks, implying prolonged carbonization. Feedstock particle size influenced peak intensities, exhibiting a nuanced effect depending on residence time, uncovering complex interactions in the GO synthesis process.

- BET and N_2 adsorption/desorption isotherm analyses elucidated the impact of process parameters on the surface area and pore structure of the GLC materials. Smaller feedstock particle sizes and higher microwave power levels were found to enhance surface area and total pore volume, contributing to improved micropore properties. However, prolonged residence times led to a reduction in these

parameters due to the softening of volatile fractions and the formation of an intermediate melt, which closed and sealed off some pores.

- Elemental analysis revealed substantial impacts of process parameters on carbon and hydrogen content, with minimal effects on sulfur and nitrogen. Microwave power levels notably raised carbon content in 60-minute residence time samples but lowered it in 90-minute residence time samples due to gas-forming reactions. Prolonged residence time resulted in decreased carbon content through volatilization. Feedstock particle size influenced carbon and hydrogen content, with larger particles favoring increased carbon in 60-minute residence time samples. The observed H/C ratios below 0.16 in all samples indicated aromatic characteristics, underscoring the significance of oxygen-containing functional group decomposition in the formation of aromatic compounds.

- SEM images revealed the sheet-like structure characteristic of GO, along with the presence of impurities such as iron oxide/carbide. The surface morphology was found to be smoother for samples with a 60-minute residence time, while an extended residence time of 90 minutes resulted in rougher surfaces with visible irregularities and pore blockage.

The key findings of this study are presented in Figure 28.

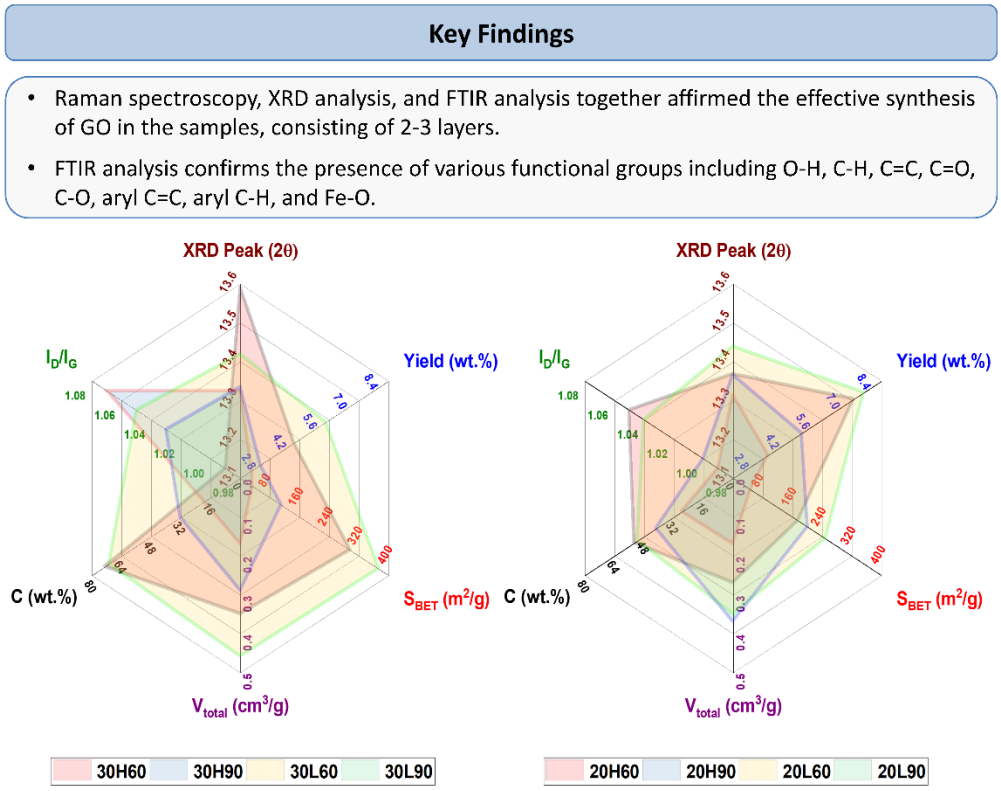

Figure 28: Key findings of the study.

5.2 Recommendations

Based on the findings, the following recommendations are proposed for future research and process optimization:

Optimization of Process Parameters: Further optimization studies could be conducted to identify the optimal combination of microwave power, residence time, and feedstock particle size for maximizing GLC yield and improving material properties. This could involve a more extensive experimental design, including additional levels of parameters.

Scale-Up Studies: The scalability of the microwave pyrolysis process should be investigated to assess its feasibility for large-scale production of GLC materials. Process parameters should be optimized for scalability while maintaining material quality.

Purification Techniques: The presence of impurities, especially iron oxide/carbide, suggests the need for purification techniques. Exploring methods such as sulfonation could be beneficial in removing these impurities and enhancing the purity of the synthesized graphene-like carbon materials.

Effect of Catalysts: Exploring the use of different catalysts with different concentrations during the microwave pyrolysis process may enhance the synthesis of GLC materials. Catalysts can influence reaction pathways, alter material properties, and potentially improve yields.

Detailed Characterization Techniques: Employing more advanced characterization techniques, such as transmission electron microscopy (TEM) and atomic force microscopy (AFM), could provide a finer resolution of the morphological features and structural details of the synthesized GLC materials.

Application Studies: Investigating the practical applications of the synthesized GLC materials, such as in energy storage devices, sensors, composite materials, or fire-resistant building materials/coatings, would validate their potential and contribute to the broader field of GLC materials applications.

Environmental Impact Assessment: Conducting an environmental impact assessment of the microwave pyrolysis process for hemp biomass, including energy consumption and emissions, could provide valuable insights into the sustainability of the synthesis method.

In conclusion, this research contributes valuable insights into the microwave pyrolysis of hemp biomass for the synthesis of GLC materials. The findings lay the foundation for further research aimed at scaling up the synthesis process, understanding underlying mechanisms, and exploring diverse applications for the synthesized materials, including the composite building materials.

Bibliography

[1] Banskota, A. H., Jones, A., Hui, J. P. M., and Stefanova, R., 2022, "Triacylglycerols and Other Lipids Profiling of Hemp By-Products," Molecules, **27**(7), p. 2339.

[2] Wallace, C. A., Afzal, M. T., and Saha, G. C., 2019, "Effect of Feedstock and Microwave Pyrolysis Temperature on Physio-Chemical and Nano-Scale Mechanical Properties of Biochar," Bioresour Bioprocess, **6**(1), p. 33.

[3] Azahar, A. A., Nurhafizah, M. D., Omar, M. R., Abdullah, N., and Ul-Hamid, A., 2022, "Bio-Graphene Production from Oil Palm Shell Waste Valorised through Sequential Thermal and Catalytic Means," Carbon Trends, **9**, p. 100225.

[4] Raghavan, N., Thangavel, S., and Venugopal, G., 2017, "A Short Review on Preparation of Graphene from Waste and Bioprecursors," Appl Mater Today, **7**, pp. 246–254.

[5] Hossain, M. Z., Sutradhar, S., and Karim, M. R., 2022, "Synthesis Method of Hemp-Derived Graphene," Journal of Scientific Research, **14**(2), pp. 601–606.

[6] Wang, H., Xu, Z., Kohandehghan, A., Li, Z., Cui, K., Tan, X., Stephenson, T. J., King'ondu, C. K., Holt, C. M. B., Olsen, B. C., Tak, J. K., Harfield, D., Anyia, A. O., and Mitlin, D., 2013, "Interconnected Carbon Nanosheets Derived from Hemp for Ultrafast Supercapacitors with High Energy," ACS Nano, **7**(6), pp. 5131–5141.

[7] Kong, X., Zhu, Y., Lei, H., Wang, C., Zhao, Y., Huo, E., Lin, X., Zhang, Q., Qian, M., Mateo, W., Zou, R., Fang, Z., and Ruan, R., 2020, "Synthesis of Graphene-like Carbon from Biomass Pyrolysis and Its Applications," Chemical Engineering Journal, **399**, p. 125808.

[8] Ivanovskii, A. L., 2012, “Graphene-Based and Graphene-like Materials,” Russian Chemical Reviews, **81**(7), pp. 571–605.

[9] Asif, F. C., and Saha, G. C., 2023, “Graphene-like Carbon Structure Synthesis from Biomass Pyrolysis: A Critical Review on Feedstock–Process–Properties Relationship,” C (Basel), **9**(1), p. 31.

[10] Zhang, J., Tahmasebi, A., Omoriyekomwan, J. E., and Yu, J., 2018, “Direct Synthesis of Hollow Carbon Nanofibers on Bio-Char during Microwave Pyrolysis of Pine Nut Shell,” J Anal Appl Pyrolysis, **130**, pp. 142–148.

[11] Debbarma, J., Naik, M. J. P., and Saha, M., 2019, “From Agrowaste to Graphene Nanosheets: Chemistry and Synthesis,” Fullerenes, Nanotubes and Carbon Nanostructures, **27**(6), pp. 482–485.

[12] Esohe Omoriyekomwan, J., Tahmasebi, A., Zhang, J., and Yu, J., 2022, “Synthesis of Super-Long Carbon Nanotubes from Cellulosic Biomass under Microwave Radiation,” Nanomaterials, **12**(5), p. 737.

[13] Somanathan, T., Prasad, K., Ostrikov, K., Saravanan, A., and Krishna, V., 2015, “Graphene Oxide Synthesis from Agro Waste,” Nanomaterials, **5**(2), pp. 826–834.

[14] Hidalgo, P., Navia, R., Hunter, R., Coronado, G., and Gonzalez, M., 2019, “Synthesis of Carbon Nanotubes Using Biochar as Precursor Material under Microwave Irradiation,” J Environ Manage, **244**, pp. 83–91.

[15] Hashmi, A., Singh, A. K., Jain, B., and Singh, A., 2020, “Muffle Atmosphere Promoted Fabrication of Graphene Oxide Nanoparticle by Agricultural Waste,” Fullerenes, Nanotubes and Carbon Nanostructures, **28**(8), pp. 627–636.

[16] Wang, Y., Srinivasakannan, C., Wang, H., Xue, G., Wang, L., Wang, X., and Duan, X., 2022, "Preparation of Novel Biochar Containing Graphene from Waste Bamboo with High Methylene Blue Adsorption Capacity," Diam Relat Mater, **125**, p. 109034.

[17] Liu, F., Chen, Y., and Gao, J., 2017, "Preparation and Characterization of Biobased Graphene from Kraft Lignin," Bioresources, **12**(3).

[18] Gopalakrishnan, A., Kong, C. Y., and Badhulika, S., 2019, "Scalable, Large-Area Synthesis of Heteroatom-Doped Few-Layer Graphene-like Microporous Carbon Nanosheets from Biomass for High-Capacitance Supercapacitors," New Journal of Chemistry, **43**(3), pp. 1186–1194.

[19] Suriapparao, D. V., Pradeep, N., and Vinu, R., 2015, "Bio-Oil Production from *Prosopis Juliflora* via Microwave Pyrolysis," Energy & Fuels, **29**(4), pp. 2571–2581.

[20] Robinson, J., Binner, E., Vallejo, D. B., Perez, N. D., al Mughairi, K., Ryan, J., Shepherd, B., Adam, M., Budarin, V., Fan, J., Gronnow, M., and Peneranda-Foix, F., 2022, "Unravelling the Mechanisms of Microwave Pyrolysis of Biomass," Chemical Engineering Journal, **430**, p. 132975.

[21] González, Z., Acevedo, B., Predeanu, G., Axinte, S. M., Drăgoescu, M.-F., Slăvescu, V., Fernandez, J. J., Granda, M., Gryglewicz, G., and Melendi-Espina, S., 2021, "Graphene Materials from Microwave-Derived Carbon Precursors," Fuel Processing Technology, **217**, p. 106803.

[22] Chen, P., Xie, Q., Addy, M., Zhou, W., Liu, Y., Wang, Y., Cheng, Y., Li, K., and Ruan, R., 2016, "Utilization of Municipal Solid and Liquid Wastes for Bioenergy and Bioproducts Production," Bioresour Technol, **215**, pp. 163–172.

[23] Omoriyekomwan, J. E., Tahmasebi, A., Zhang, J., and Yu, J., 2017, "Formation of Hollow Carbon Nanofibers on Bio-Char during Microwave Pyrolysis of Palm Kernel Shell," Energy Convers Manag, **148**, pp. 583–592.

[24] Shi, K., Yan, J., Lester, E., and Wu, T., 2014, "Catalyst-Free Synthesis of Multiwalled Carbon Nanotubes via Microwave-Induced Processing of Biomass," Ind Eng Chem Res, **53**(39), pp. 15012–15019.

[25] Huang, Y. F., Kuan, W. H., Lo, S. L., and Lin, C. F., 2008, "Total Recovery of Resources and Energy from Rice Straw Using Microwave-Induced Pyrolysis," Bioresour Technol, **99**(17), pp. 8252–8258.

[26] Parthasarathy, P., and Sheeba, K. N., 2017, "Generation of Fuel Char through Biomass Slow Pyrolysis," Energy Sources, Part A: Recovery, Utilization, and Environmental Effects, **39**(6), pp. 599–605.

[27] Huang, Y.-F., Chiueh, P.-T., Kuan, W.-H., and Lo, S.-L., 2016, "Microwave Pyrolysis of Lignocellulosic Biomass: Heating Performance and Reaction Kinetics," Energy, **100**, pp. 137–144.

[28] Liu, H., E, J., Deng, Y., Xie, C., and Zhu, H., 2016, "Experimental Study on Pyrolysis Characteristics of the Tobacco Stem Based on Microwave Heating Method," Appl Therm Eng, **106**, pp. 473–479.

[29] Kan, T., Strezov, V., and Evans, T. J., 2016, “Lignocellulosic Biomass Pyrolysis: A Review of Product Properties and Effects of Pyrolysis Parameters,” Renewable and Sustainable Energy Reviews, **57**, pp. 1126–1140.

[30] Demirbas, A., 2004, “Effect of Initial Moisture Content on the Yields of Oily Products from Pyrolysis of Biomass,” J Anal Appl Pyrolysis, **71**(2), pp. 803–815.

[31] Liu, H., Zhang, Q., Hu, H., Li, A., and Yao, H., 2014, “Influence of Residual Moisture on Deep Dewatered Sludge Pyrolysis,” Int J Hydrogen Energy, **39**(3), pp. 1253–1261.

[32] Gray, M. R., Corcoran, W. H., and Gavalas, G. R., 1985, “Pyrolysis of a Wood-Derived Material. Effects of Moisture and Ash Content,” Industrial & Engineering Chemistry Process Design and Development, **24**(3), pp. 646–651.

[33] Westerhof, R. J. M., Kuipers, N. J. M., Kersten, S. R. A., and van Swaaij, W. P. M., 2007, “Controlling the Water Content of Biomass Fast Pyrolysis Oil,” Ind Eng Chem Res, **46**(26), pp. 9238–9247.

[34] Fonseca, F. G., Funke, A., Niebel, A., Soares Dias, A. P., and Dahmen, N., 2019, “Moisture Content as a Design and Operational Parameter for Fast Pyrolysis,” J Anal Appl Pyrolysis, **139**, pp. 73–86.

[35] Darmstadt, H., Pantea, D., Sümmchen, L., Roland, U., Kaliaguine, S., and Roy, C., 2000, “Surface and Bulk Chemistry of Charcoal Obtained by Vacuum Pyrolysis of Bark: Influence of Feedstock Moisture Content,” J Anal Appl Pyrolysis, **53**(1), pp. 1–17.

[36] Li, X., Peng, B., Liu, Q., and Zhang, H., 2022, “Microwave Pyrolysis Coupled with Conventional Pre-Pyrolysis of the Stalk for Syngas and Biochar,” Bioresour Technol, **348**, p. 126745.

[37] Jian, J., Lu, Z., Yao, S., Li, Y., Liu, Z., Lang, B., and Chen, Z., 2019, “Effects of Thermal Conditions on Char Yield and Char Reactivity of Woody Biomass in Stepwise Pyrolysis,” J Anal Appl Pyrolysis, **138**, pp. 211–217.

[38] Leite, J. C. S., Suota, M. J., Ramos, L. P., Lenzi, M. K., and de Lima Luz, L. F., 2022, “Depolymerization of Sugarcane Bagasse by Microwave-Assisted Pyrolysis,” Chem Eng Trans, **92**, pp. 511–516.

[39] Burhenne, L., Damiani, M., and Aicher, T., 2013, “Effect of Feedstock Water Content and Pyrolysis Temperature on the Structure and Reactivity of Spruce Wood Char Produced in Fixed Bed Pyrolysis,” Fuel, **107**, pp. 836–847.

[40] van de Velden, M., Baeyens, J., Brems, A., Janssens, B., and Dewil, R., 2010, “Fundamentals, Kinetics and Endothermicity of the Biomass Pyrolysis Reaction,” Renew Energy, **35**(1), pp. 232–242.

[41] Safdari, M.-S., Amini, E., Weise, D. R., and Fletcher, T. H., 2019, “Heating Rate and Temperature Effects on Pyrolysis Products from Live Wildland Fuels,” Fuel, **242**, pp. 295–304.

[42] Gerçel, H. F., 2011, “Bio-Oil Production from Onopordum Acanthium L. by Slow Pyrolysis,” J Anal Appl Pyrolysis, **92**(1), pp. 233–238.

[43] Asadullah, M., Zhang, S., and Li, C.-Z., 2010, “Evaluation of Structural Features of Chars from Pyrolysis of Biomass of Different Particle Sizes,” Fuel Processing Technology, **91**(8), pp. 877–881.

[44] Fu, P., Hu, S., Xiang, J., Sun, L., Su, S., and Wang, J., 2012, “Evaluation of the Porous Structure Development of Chars from Pyrolysis of Rice Straw: Effects of Pyrolysis Temperature and Heating Rate,” J Anal Appl Pyrolysis, **98**, pp. 177–183.

[45] Zhao, B., O’Connor, D., Zhang, J., Peng, T., Shen, Z., Tsang, D. C. W., and Hou, D., 2018, “Effect of Pyrolysis Temperature, Heating Rate, and Residence Time on Rapeseed Stem Derived Biochar,” J Clean Prod, **174**, pp. 977–987.

[46] Lua, A. C., 2020, “A Detailed Study of Pyrolysis Conditions on the Production of Steam-Activated Carbon Derived from Oil-Palm Shell and Its Application in Phenol Adsorption,” Biomass Convers Biorefin, **10**(2), pp. 523–533.

[47] Kumar, M., and Gupta, R. C., 1994, “Influence of Carbonization Conditions on the Gasification of Acacia and Eucalyptus Wood Chars by Carbon Dioxide,” Fuel, **73**(12), pp. 1922–1925.

[48] Yu, J., Sun, L., Berrueco, C., Fidalgo, B., Paterson, N., and Millan, M., 2018, “Influence of Temperature and Particle Size on Structural Characteristics of Chars from Beechwood Pyrolysis,” J Anal Appl Pyrolysis, **130**, pp. 127–134.

[49] Zeng, K., Minh, D. P., Gauthier, D., Weiss-Hortala, E., Nzihou, A., and Flamant, G., 2015, “The Effect of Temperature and Heating Rate on Char Properties Obtained from Solar Pyrolysis of Beech Wood,” Bioresour Technol, **182**, pp. 114–119.

[50] Antal, M. J., and Grønli, M., 2003, “The Art, Science, and Technology of Charcoal Production,” Ind Eng Chem Res, **42**(8), pp. 1619–1640.

[51] Lu, G. Q., Low, J. C. F., Liu, C. Y., and Lua, A. C., 1995, “Surface Area Development of Sewage Sludge during Pyrolysis,” Fuel, **74**(3), pp. 344–348.

[52] Zhang, Y., Wu, W., Zhao, S., Long, Y., and Luo, Y., 2015, “Experimental Study on Pyrolysis Tar Removal over Rice Straw Char and Inner Pore Structure Evolution of Char,” Fuel Processing Technology, **134**, pp. 333–344.

[53] Ethaib, S., Omar, R., Kamal, S. M. M., Awang Biak, D. R., and Zubaidi, S. L., 2020, “Microwave-Assisted Pyrolysis of Biomass Waste: A Mini Review,” Processes, **8**(9), p. 1190.

[54] Fang, Z., Gao, Y., Bolan, N., Shaheen, S. M., Xu, S., Wu, X., Xu, X., Hu, H., Lin, J., Zhang, F., Li, J., Rinklebe, J., and Wang, H., 2020, “Conversion of Biological Solid Waste to Graphene-Containing Biochar for Water Remediation: A Critical Review,” Chemical Engineering Journal, **390**, p. 124611.

[55] Safian, M. T., Haron, U. S., and Mohamad Ibrahim, M. N., 2020, “A Review on Bio-Based Graphene Derived from Biomass Wastes,” Bioresources, **15**(4), pp. 9756–9785.

[56] 2020, “Chemistry and Mechanism of One-Step Formation of Graphene from Agrowaste,” Letters in Applied NanoBioScience, **9**(3), pp. 1389–1394.

[57] Debbarma, J., Mandal, P., and Saha, M., 2020, “N-Graphene Oxide and N-Reduced Graphene Oxide from Jujube Seeds: Chemistry and Mechanism,” Fullerenes, Nanotubes and Carbon Nanostructures, **28**(9), pp. 702–706.

[58] Roy, A., Kar, S., Ghosal, R., Naskar, K., and Bhowmick, A. K., 2021, "Facile Synthesis and Characterization of Few-Layer Multifunctional Graphene from Sustainable Precursors by Controlled Pyrolysis, Understanding of the Graphitization Pathway, and Its Potential Application in Polymer Nanocomposites," ACS Omega, **6**(3), pp. 1809–1822.

[59] Omoriyekomwan, J. E., Tahmasebi, A., Zhang, J., and Yu, J., 2019, "Mechanistic Study on Direct Synthesis of Carbon Nanotubes from Cellulose by Means of Microwave Pyrolysis," Energy Convers Manag, **192**, pp. 88–99.

[60] Omoriyekomwan, J. E., Tahmasebi, A., Dou, J., Wang, R., and Yu, J., 2021, "A Review on the Recent Advances in the Production of Carbon Nanotubes and Carbon Nanofibers via Microwave-Assisted Pyrolysis of Biomass," Fuel Processing Technology, **214**, p. 106686.

[61] Tan, H., Wang, D., and Guo, Y., 2018, "Thermal Growth of Graphene: A Review," Coatings, **8**(1), p. 40.

[62] Wang, N., Tahmasebi, A., Yu, J., Xu, J., Huang, F., and Mamaeva, A., 2015, "A Comparative Study of Microwave-Induced Pyrolysis of Lignocellulosic and Algal Biomass," Bioresour Technol, **190**, pp. 89–96.

[63] Li, J., Dai, J., Liu, G., Zhang, H., Gao, Z., Fu, J., He, Y., and Huang, Y., 2016, "Biochar from Microwave Pyrolysis of Biomass: A Review," Biomass Bioenergy, **94**, pp. 228–244.

[64] Mbayachi, V. B., Ndayiragije, E., Sammani, T., Taj, S., Mbuta, E. R., and khan, A. ullah, 2021, "Graphene Synthesis, Characterization and Its Applications: A Review," Results Chem, **3**, p. 100163.

[65] Hu, M., Yao, Z., and Wang, X., 2017, "Characterization Techniques for Graphene-Based Materials in Catalysis," AIMS Mater Sci, **4**(3), pp. 755–788.

[66] Ferrari, A. C., and Robertson, J., 2000, "Interpretation of Raman Spectra of Disordered and Amorphous Carbon," Phys Rev B, **61**(20), pp. 14095–14107.

[67] Athanasiou, M., Yannopoulos, S. N., and Ioannides, T., 2022, "Biomass-Derived Graphene-like Materials as Active Electrodes for Supercapacitor Applications: A Critical Review," Chemical Engineering Journal, **446**, p. 137191.

[68] Hidayah, N. M. S., Liu, W.-W., Lai, C.-W., Noriman, N. Z., Khe, C.-S., Hashim, U., and Lee, H. C., 2017, "Comparison on Graphite, Graphene Oxide and Reduced Graphene Oxide: Synthesis and Characterization," p. 150002.

[69] Bunaciu, A. A., Udriştioiu, E. gabriela, and Aboul-Enein, H. Y., 2015, "X-Ray Diffraction: Instrumentation and Applications," Crit Rev Anal Chem, **45**(4), pp. 289–299.

[70] Li, C., Hayashi, J., Sun, Y., Zhang, L., Zhang, S., Wang, S., and Hu, X., 2021, "Impact of Heating Rates on the Evolution of Function Groups of the Biochar from Lignin Pyrolysis," J Anal Appl Pyrolysis, **155**, p. 105031.

[71] ISO, ISO/TS 21356-1:2021 Nanotechnologies - Structural characterization of graphene - Part 1: Graphene from powders and dispersions, (2021).

[72] Gnanaraj, J. M. S., Kumar, G. S., Pandian, M. S., Ramasamy, P., Varuna, K., and Kumar, S. S., 2022, "Facile Synthesis of Reduced Graphene Oxide from Azadirachta Indica for Optical Power Limiting Applications: An Eco-Friendly Approach," Journal of Materials Science: Materials in Electronics, **33**(26), pp. 20631–20641.

[73] Thangaraj, B., Mumtaz, F., Abbas, Y., Anjum, D. H., Solomon, P. R., and Hassan, J., 2023, "Synthesis of Graphene Oxide from Sugarcane Dry Leaves by Two-Stage Pyrolysis," Molecules, **28**(8), p. 3329.

[74] Kashinath, L., Namratha, K., and Byrappa, K., 2016, "Microwave Assisted Synthesis and Characterization of Nanostructure Zinc Oxide-Graphene Oxide and Photo Degradation of Brilliant Blue," Mater Today Proc, **3**(1), pp. 74–83.

[75] Zhi, M., Liu, Q., Chen, H., Feng, S., and He, Y., 2019, "Study on Efficient and Green Reduction of Graphene Oxide by a One-Step Hydrothermal Method," J Phys Conf Ser, **1213**(5), p. 052047.

[76] Kumar, N., and Srivastava, V. C., 2018, "Simple Synthesis of Large Graphene Oxide Sheets via Electrochemical Method Coupled with Oxidation Process," ACS Omega, **3**(8), pp. 10233–10242.

[77] Yogesh, G. K., Shuaib, E. P., Roopmani, P., Gumpu, M. B., Krishnan, U. M., and Sastikumar, D., 2020, "Synthesis, Characterization and Bioimaging Application of Laser-Ablated Graphene-Oxide Nanoparticles (NGOs)," Diam Relat Mater, **104**, p. 107733.

[78] Haghighi, B., and Tabrizi, M. A., 2013, “Green-Synthesis of Reduced Graphene Oxide Nanosheets Using Rose Water and a Survey on Their Characteristics and Applications,” RSC Adv, **3**(32), p. 13365.

[79] Liu, W.-J., Tian, K., He, Y.-R., Jiang, H., and Yu, H.-Q., 2014, “High-Yield Harvest of Nanofibers/Mesoporous Carbon Composite by Pyrolysis of Waste Biomass and Its Application for High Durability Electrochemical Energy Storage,” Environ Sci Technol, **48**(23), pp. 13951–13959.

[80] Tinh, N. T., Phuong, N. T., Nghiem, D. G., Dan, D. K., Khang, P. T., Dat, N. M., Vy, H. T. T., Huong, L. M., Hoang, T. M., Phong, M. T., and Hieu, N. H., 2022, “Green Synthesis of Sulfonated Graphene Oxide-like Catalyst from Corncob for Conversion of Hemicellulose into Furfural,” Biomass Convers Biorefin.

[81] Özbay, N., Yargıç, A. Ş., Yaman, E., Yarbay, R. Z., Dermenci, K. B., and Turan, S., 2023, “Production of Si-Doped Biomass-Derived Materials: Effect of Support Type, Activation and Doping Conditions,” Biomass Convers Biorefin.

[82] Choi, Y.-K., Jang, H. M., Kan, E., Wallace, A. R., and Sun, W., 2018, “Adsorption of Phosphate in Water on a Novel Calcium Hydroxide-Coated Dairy Manure-Derived Biochar,” Environmental Engineering Research, **24**(3), pp. 434–442.

[83] Ostermann, M., Velicsanyi, P., Bilotto, P., Schodl, J., Nadlinger, M., Fafilek, G., Lieberzeit, P. A., and Valtiner, M., 2022, “Development and Up-Scaling of Electrochemical Production and Mild Thermal Reduction of Graphene Oxide,” Materials, **15**(13), p. 4639.

[84] Ţucureanu, V., Matei, A., and Avram, A. M., 2016, "FTIR Spectroscopy for Carbon Family Study," Crit Rev Anal Chem, **46**(6), pp. 502–520.

[85] Dimiev, A. M., and Polson, T. A., 2015, "Contesting the Two-Component Structural Model of Graphene Oxide and Reexamining the Chemistry of Graphene Oxide in Basic Media," Carbon N Y, **93**, pp. 544–554.

[86] Eigler, S., Dotzer, C., Hirsch, A., Enzelberger, M., and Müller, P., 2012, "Formation and Decomposition of CO_2 Intercalated Graphene Oxide," Chemistry of Materials, **24**(7), pp. 1276–1282.

[87] Haeldermans, T., Claesen, J., Maggen, J., Carleer, R., Yperman, J., Adriaensens, P., Samyn, P., Vandamme, D., Cuypers, A., Vanreppelen, K., and Schreurs, S., 2019, "Microwave Assisted and Conventional Pyrolysis of MDF – Characterization of the Produced Biochars," J Anal Appl Pyrolysis, **138**, pp. 218–230.

[88] Ludwig, V., de Lima, A. H., Modesto-Costa, L., Da Costa Ludwig, Z. M., de Mendonça, J. P. A., Quirino, W. G., and Sato, F., 2021, "Experimental and Theoretical Study of Solvent Effect in Graphene Oxide," J Mol Liq, **342**, p. 117429.

[89] Dimiev, A. M., Alemany, L. B., and Tour, J. M., 2013, "Graphene Oxide. Origin of Acidity, Its Instability in Water, and a New Dynamic Structural Model," ACS Nano, **7**(1), pp. 576–588.

[90] Wang, H., and Hu, Y. H., 2013, "Electrolyte-Induced Precipitation of Graphene Oxide in Its Aqueous Solution," J Colloid Interface Sci, **391**, pp. 21–27.

[91] Chen, Y., Tian, G., Liang, H., and Liang, Y., 2019, "Synthesis of Magnetically Responsive Hyperbranched Polyamidoamine Based on the Graphene Oxide:

Application as Demulsifier for Oil-in-water Emulsions," Int J Energy Res, **43**(9), pp. 4756–4765.

[92] Lu, L., 2002, "Char Structural Ordering during Pyrolysis and Combustion and Its Influence on Char Reactivity," Fuel, **81**(9), pp. 1215–1225.

[93] Wang, B., Hu, J., Chen, W., Chang, C., Pang, S., and Li, P., 2024, "Exploring the Characteristics of Coke Formation on Biochar-Based Catalysts during the Biomass Pyrolysis," Fuel, **357**, p. 129859.

[94] Hu, Z., Srinivasan, M. P., and Ni, Y., 2001, "Novel Activation Process for Preparing Highly Microporous and Mesoporous Activated Carbons," Carbon N Y, **39**(6), pp. 877–886.

[95] Burwell, R. L., 1977, "Manual of Symbols and Terminology for Physicochemical Quantities and Units—Appendix II Heterogeneous Catalysis," pp. 351–392.

[96] Chen, C., Li, X., Tong, Z., Li, Y., and Li, M., 2014, "Modification Process Optimization, Characterization and Adsorption Property of Granular Fir-Based Activated Carbon," Appl Surf Sci, **315**, pp. 203–211.

[97] Li, Y., Xing, B., Wang, X., Wang, K., Zhu, L., and Wang, S., 2019, "Nitrogen-Doped Hierarchical Porous Biochar Derived from Corn Stalks for Phenol-Enhanced Adsorption," Energy & Fuels, **33**(12), pp. 12459–12468.

[98] Lua, A. C., Yang, T., and Guo, J., 2004, "Effects of Pyrolysis Conditions on the Properties of Activated Carbons Prepared from Pistachio-Nut Shells," J Anal Appl Pyrolysis, **72**(2), pp. 279–287.

[99] Yang, H., Coolman, R., Karanjkar, P., Wang, H., Dornath, P., Chen, H., Fan, W., Conner, W. C., Mountziaris, T. J., and Huber, G., 2017, "The Effects of Contact Time and Coking on the Catalytic Fast Pyrolysis of Cellulose," Green Chemistry, **19**(1), pp. 286–297.

[100] Nazem, M. A., Zare, M. H., and Shirazian, S., 2020, "Preparation and Optimization of Activated Nano-Carbon Production Using Physical Activation by Water Steam from Agricultural Wastes," RSC Adv, **10**(3), pp. 1463–1475.

[101] Liu, R., Liu, G., Yousaf, B., and Abbas, Q., 2018, "Operating Conditions-Induced Changes in Product Yield and Characteristics during Thermal-Conversion of Peanut Shell to Biochar in Relation to Economic Analysis," J Clean Prod, **193**, pp. 479–490.

[102] Tripathi, M., Bhatnagar, A., Mubarak, N. M., Sahu, J. N., and Ganesan, P., 2020, "RSM Optimization of Microwave Pyrolysis Parameters to Produce OPS Char with High Yield and Large BET Surface Area," Fuel, **277**, p. 118184.

[103] Veiga, P. A. da S., Schultz, J., Matos, T. T. da S., Fornari, M. R., Costa, T. G., Meurer, L., and Mangrich, A. S., 2020, "Production of High-Performance Biochar Using a Simple and Low-Cost Method: Optimization of Pyrolysis Parameters and Evaluation for Water Treatment," J Anal Appl Pyrolysis, **148**, p. 104823.

[104] Suriapparao, D. V., and Vinu, R., 2021, "Recovery of Renewable Carbon Resources from the Household Kitchen Waste via Char Induced Microwave Pyrolysis," Renew Energy, **179**, pp. 370–378.

[105] de Souza Souza, C., Bomfim, M. R., Conceição de Almeida, M. da, Alves, L. de S., de Santana, W. N., da Silva Amorim, I. C., and Santos, J. A. G., 2021, "Induced Changes of Pyrolysis Temperature on the Physicochemical Traits of Sewage Sludge and on the Potential Ecological Risks," Sci Rep, **11**(1), p. 974.

[106] Huang, Y., Zeng, M., Ren, J., Wang, J., Fan, L., and Xu, Q., 2012, "Preparation and Swelling Properties of Graphene Oxide/Poly(Acrylic Acid-Co-Acrylamide) Super-Absorbent Hydrogel Nanocomposites," Colloids Surf A Physicochem Eng Asp, **401**, pp. 97–106.

Curriculum Vitae

Candidate's full name: Farhan Chowdhury Asif

Universities attended: Military Institute of Science & Technology, Dhaka, Bangladesh, B.Sc. in Mechanical Engineering (2015 – 2019)

Publications:

1. Asif, F.C., Saha, G.C. Graphene-like Carbon Structure Synthesis from Biomass Pyrolysis: A Critical Review on Feedstock–Process–Properties Relationship. C 2023, 9, 31. https://doi.org/10.3390/c9010031
2. Ahsan, M., Ahsan, P. M., Islam, M. A., & Asif, F. C. (2019). Structural and electrical properties of copper doped lanthanum manganite NPs. Results in Physics, 15, 102600. https://doi.org/10.1016/j.rinp.2019.102600

Conference Presentations:

1. Looi, T.-R., Asif, F.C., Stewart, W., Saha, G.C., Thermodynamic profile characterization of mold geometries in composite pultrusion manufacturing, Presented at the 12th Canadian-International Conference on Composites (CANCOM-2022), July 12th-15th, 2022, Fredericton-Moncton NB, Canada.